Geophys. J. Int. (1999) **138,** 601–624

Simple models for late Holocene and present-day Patagonian glacier fluctuations and predictions of a geodetically detectable isostatic response

Erik R. Ivins[1] and Thomas S. James[2]

[1] *Jet Propulsion Laboratory, California Institute of Technology,* 4800 *Oak Grove Drive, Pasadena,* CA 91109-8099, *USA.*
E-mail: eri@fryxell.jpl.nasa.gov
[2] *Geological Survey of Canada, Pacific Geoscience Centre, Sidney, BC,* V8L 4B2, *Canada*

Accepted 1999 March 25. Received 1999 February 22; in original form 1998 June 4

SUMMARY

The late Holocene glacial moraine chronology in the southernmost South American Andes includes four ^{14}C dated Neoglacial advances and retreats. These are used as proxy information to characterize mass fluctuation of the Patagonian icefields during the last 5000 years. Modelled ice loads force a phase-lagged viscoelastic gravitational deformation of the solid Earth. The ancient glacier fluctuations may, therefore, drive present-day crustal motion even in the absence of present-day ice mass imbalance. Numerical models show that such rates of present-day uplift and subsidence are larger than those driven by the viscous memory of late Pleistocene deglaciation. Both spherical and flat-earth models are employed, the latter being used to study exhaustively the e ects of glacial load history on the predicted vertical crustal velocity. Recent assessment of net mass balance from 1944 to 1985 indicates that the Southern Patagonian icefield has significantly deteriorated due to snout retreat and thinning. Volume loss rates are estimated at about 3.4–9.3 $km^3\ yr^{-1}$. The predicted vertical isostatic response to this recession and to the modelled Holocene Neoglaciations is at a marginally detectable level (≈ 1 mm yr^{-1}) if the mantle/asthenosphere beneath Patagonia has a viscosity of about 10^{21} Pa s. However, for reduced mantle viscosities, the younger Holocene glacial load histories predict larger signatures. In fact, if the viscosity is about 2×10^{20} Pa s, or lower, then geodetically detectable vertical motion may be driven by a regional Little Ice Age (LIA) (1400–1750 AD) glacier advance and subsequent 20th century retreat. Although this value for mantle viscosity is lower than thought typical of continental shield mantle ($\approx 10^{21}$ Pa s), it is consistent with inversions for post-seismic relaxation time constants in island arc environments and in regions with significant Neogene continental tectonism. In the viscosity regime of 5×10^{18}–2×10^{19} Pa s, the predicted rates of vertical crustal motion are similar to those presently occurring in Fennoscandia and Hudson Bay (5–10 mm yr^{-1}). Geodetic data may be sensitive to the time-integrated growth and subsequent retreat of Patagonian glacier ice mass over the last 600 years.

Key words: crustal deformation, geodesy, glacial rebound, hydrology, mantle rheology.

1 INTRODUCTION

Recent evaluation of the 20th century mass balance of the Northern and Southern Patagonian Icefields (NPI and SPI, respectively) has determined that both are in a prolonged state of recession that continues to the present day (Aniya 1988; Naruse *et al.* 1995; Aniya *et al.* 1996). A compilation of mass-balance-related information has been published and summarized by Aniya *et al.* (1997). This information includes a wealth of satellite and airborne imagery that complements ground-based glaciological data. Aniya *et al.* (1997) concluded that the total volume change for the SPI during the time span 1945–1986 is 140–380 km^3. This rate of glacial recession is substantial, amounting to about 3–5 per cent of the total global estimate made by Meier (1984) ($\approx 0.46 \pm 0.26$ mm yr^{-1} in sea level rise equivalent) for the rate at which mass was lost from the world's

mountain glacier systems during the period 1900–1961. Rapid vertical movement might accompany this glacial retreat due to the solid Earth's elastic–gravitational response, and this crustal deformation might be detected using high-quality Global Positioning System (GPS) station data.

The viscoelastic response of the Earth is a serious complication, however, since past glacial advancement and/or retreat a ect the present-day crustal response. Fennoscandian and Hudson Bay uplift represent classic examples of the Earth's long-term memory of past glacial loading. A well-documented Little Ice Age glacial advance (Mercer 1970, 1976, 1982; Rabassa & Clapperton 1990; Aniya 1995) of somewhat uncertain timing (circa 1400–1750 AD) and two–three additional Neoglacial oscillations of late Holocene age (1–5 kyr BP) might be preserved in the viscously 'sluggish' isostatic memory of the mantle/lithosphere.

The main goal of this paper is to examine the sensitivity of the predicted present-day vertical crustal response to three factors: (i) ongoing and well-documented 20th century Patagonian glacial recession (Aniya 1988; Naruse *et al.* 1995; Aniya *et al.* 1997); (ii) pre-20th century palaeo-icefield reconstructions that can be partially constrained by ^{14}C dated moraine sequences; (iii) variations in viscoelastic earth model parameters. Towards this end a simple and computationally e cient method for calculation of the viscoelastic response with an elastic lithosphere and a Maxwell half-space is presented. The mathematical formulation follows that of Wolf (1985a) and is well suited to complex load histories. Although lithospheric thickness is important, the viscosity assumed for the half-space is the more fundamental mechanical parameter influencing the predictions of present-day vertical rates.

The Patagonian icefields are found in a unique tectonic environment, one that has experienced the creation of a mantle slab window, left in the wake of the northward migration of the Chile triple junction and subduction of an active oceanic ridge during the past 12 Myr (Gorring *et al.* 1997). High heat flow, late Tertiary–Quaternary volcanism and the subduction of ocean ridge segments during the past 15 Myr (Hamza & Muñoz 1996; Gorring *et al.* 1997) suggest a mantle viscosity that should be substantially lower than 10^{21} Pa s. During the late Miocene (17–14 Ma) robust mountain building processes were operative in the region now occupied by the icefields, but these have substantially waned since that time (Ramos & Kay 1992). We demonstrate that if the upper mantle viscosity is lower than that determined from the analysis of raised beaches in Fennoscandia by a factor of 0.2 to 0.01, then vertical motions caused by a 'Little Ice Age' glacial rebound are large enough to be detected using space geodetic methods.

2 OBSERVATIONS OF GLACIER FLUCTUATION

The extent of the Northern and Southern Patagonian icefields is shown in Fig. 1. These two temperate glacier systems

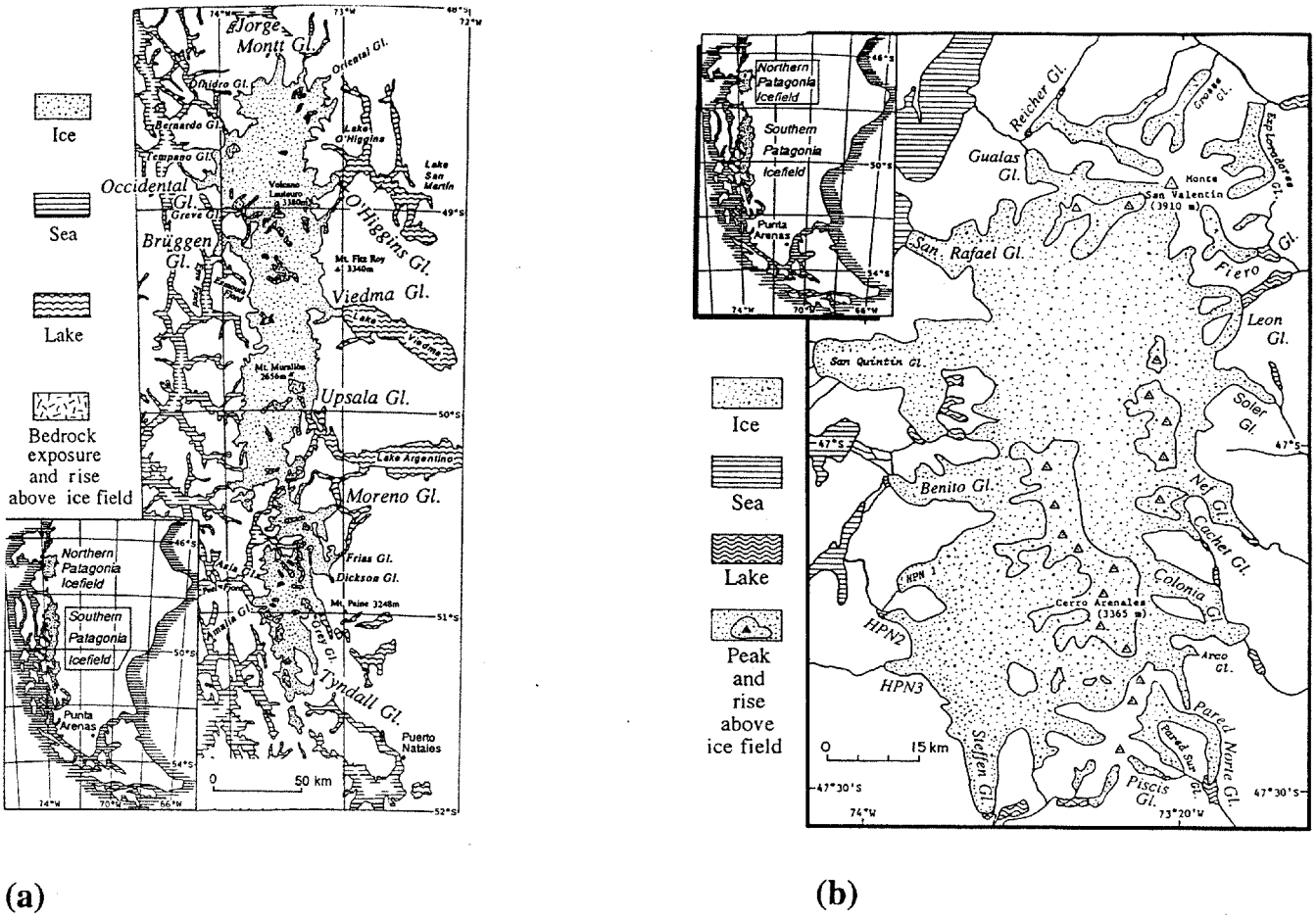

Figure 1. South (a) and North (b) Patagonia icefields (Naruse *et al.* 1995).

form the third largest continental ice complex in the world, with only Greenland and Antarctica having greater hydrological mass (Naruse & Aniya 1992; Warren & Sugden 1993). Dramatic changes in the Patagonian outlet glacier system have been documented since the beginning of the historical record (Warren 1993; Warren & Sugden 1993). Within the past decade new quantitative estimates of the mass balance of both the NPI (Aniya 1988) and the SPI (Aniya *et al.* 1997) have emerged.

2.1 Mid- to Late 20th century changes

Evaluation of mid- to late 20th century total mass balance of the Patagonian ice fields has been accomplished by using a combination of ground surveys and aerial photographs, including oblique Space Shuttle photos and cloud-free LANDSAT imagery of the NPI (January 22 1979) and the SPI (January 14 1986). The results have been discussed in a series of papers by Aniya (1988), Naruse *et al.* (1995) and Aniya *et al.* (1996; 1997). Here, a total of 48 outlet glaciers of the SPI were examined utilizing a series of US Army Air Force oblique photographs taken during the summer of 1944/1945 as a basis for comparison with the glacial extent of the summer of 1985/1986. Although several SPI glaciers were found to be near equilibrium, and two in a state of advancement, 33 of the SPI glaciers show loss in area at an average rate of 0.192 $km^2\ yr^{-1}$, whilst a similar study of the NPI shows a loss rate of 0.044 $km^2\ yr^{-1}$ (Aniya *et al.* 1997). By obtaining a number of thickness estimates at the retreating snouts of outlet glaciers, an approximate volume estimate could be calculated. Some glacial thinning estimates were made from combined aerial photography and field observation, ranging from below 1 m yr^{-1} to a maximum of 4 m yr^{-1} averaged over 41 years. Aniya *et al.* (1997) concluded that the volume loss in the SPI over a 41 year time span by snout retreat was 40–80 km^3, whilst that associated with thinning was roughly 100–300 km^3. The pace of glacial recession in the SPI seems to have accelerated after the mid-1970s (Aniya *et al.* 1997). No analogous volume loss estimates for the NPI have yet been published. Thickness change measurements have not been made within the accumulation zones, and future studies might allow the net mass balance of the icefields to be improved upon (Eric Rignot, personal communication, 1999).

Atmospheric moisture that sustains icefield growth is derived almost exclusively from the prevailing Southern Westerlies. Pleistocene, Holocene and Recent glacial fluctuation is, therefore, intimately connected to the moisture content, temperature, zonal position and intensity of these Westerlies (Heusser 1989; Hulton *et al.* 1994). Atmospheric temperature variation may a ect both the growth and the shrinkage of the icefields over centennial timescales. Numerical simulation of the shrinkage of the Franz Joseph Glacier in New Zealand over the last 150 years by Oerlemans (1997) indicates that a secular warming of 0.6 °C per century could account for the observed recession from moraine maxima at 1750–1820 AD. A model of Patagonian glacial recession during the 20th century developed by Naruse *et al.* (1995) suggests that a rise in the equilibrium-line altitude of 100 m (corresponding to a 1–2 °C increase in air temperature) could explain the observed changes of the Upsala and Moreno glaciers in the SPI (see Fig. 1). The characteristic time for the mass response of alpine glaciers at this latitude is fairly short, about 15 years according to Oerlemans (1997), implying that Holocene volume changes of the Patagonian icefields are probably indicative of climate changes (Warren 1993).

2.2 Late Holocene (0–5 ka BP) moraine advances and retreats

2.2.1 *Little Ice Age (LIA)*

Mean surface air temperatures in the Southern Hemisphere appear to follow the basic 0.5–0.7 °C warming trend over that past 100–150 years that is observed in the Northern Hemisphere (Jones *et al.* 1986; Hansen & Lebede 1987). Temperature records in the latitude band from 44.4°S to 64.2°S show an average surface air temperature increase of 0.9 ± 0.3 °C from 1880 to 1940, but the number and quality of the reporting stations make inferences inadvisable according to Hansen & Lebede (1987). In Patagonia any local correlation of temperature and glacier volume change cannot be made (Warren & Sugden 1993). However, very clear evidence for glacial advancement during the LIA in Patagonia is found in the form of datable moraines. Mercer (1970, 1976) dated both forest trimlines and moraine debris and determined that widespread glacial maxima occurred during the mid-18th and mid-19th centuries. The data include a strongly tilted cypress tree found in the northwestern section of the SPI that dates the maximum advancement of the Tempano glacier to the year AD 1760 ± 10 (Mercer 1970). Glacial moraines outside the Patagonian icefields show a somewhat coincident advance during the LIA both in the Andean mountains to the north (Clapperton & Sugden 1988) and in the sub-Antarctic islands to the south (Clapperton & Sugden 1983). Mid-18th century advance of the San Rafael glacier, and subsequent recession initiating in 1880, has been documented in historical records (Warren 1993). Unfortunately, many of the dendrochronological temperature reconstructions for Patagonia show no consistent pattern of cold conditions since AD 1500, with the exception of the years AD 1532–1538 and 1556–1562 (Boninsegna 1995). An analysis of tree ring records near the northern edge of the NPI, however, reveals evidence of an extended period of cold and moist conditions from AD 1280–1670, with this trend peaking at AD 1340 and again at 1650 (Villalba 1990). For the purpose of computing present-day isostatic signatures we will take the LIA in Patagonia to be bracketed in time by AD 1400–1880.

2.2.2 *Neoglacial moraine record*

Dates on terminal moraines along both the western and eastern flanks of the southern Andes provide estimates of the timing of advances of the SPI and NPI glacier systems. The dates of various organic materials tend to yield minimum ages only, thus the derived chronologies have some uncertainty. Mercer (1970, 1976, 1982) proposed three Neoglacial advances since 5 kyr BP based upon moraine dates along the northwestern margins of the SPI. The first was dated to 4.7–4.2 and the second to 2.7–2.0 kyr BP. The third coincided with the LIA, as discussed above. Aniya (1995) later analysed data from moraines of the Tyndall and Upsala glaciers (see Fig. 1) and concluded that there have been four late Holocene Neoglacial advances, each maxima being achieved at about 3.6, 2.3, 1.6–1.4 and 0.3 kyr BP. The evidence for the third Neoglacial includes a ^{14}C date from a standing Nothofagus stump near a terminal moraine of the Tyndall glacier. Both the Neoglacial scenarios

suggested by Mercer (1970) and by Aniya (1995) will be examined to test their potential influence on present-day glacial rebound.

Fig. 2 shows an approximate method for accounting for these scenarios of late Holocene Neoglaciation and Last Glacial Maximum (LGM). Here the total volume of ice is shown as a function of time for two scenarios, one similar to that of Mercer (1970, 1976, 1982) (Type 1) and the other reminiscent of that proposed by Aniya (1995) (Type 2). An early Neoglacial at 4.5 kyr BP corresponds to numerous minimal age dates reported by Mercer (1970, 1976, 1982) and coincides with regional cooling trends suggested by Heusser & Streeter (1980). The palynological record indicates that the period 13–5 ka was marked by warm temperatures (Heusser & Streeter 1980; Rabassa & Clapperton 1990), punctuated only at 11–10 kyr BP by a Younger Dryas-like cold epoch (Heusser *et al.* 1996). Rabassa & Clapperton (1990) suggested that the icefields may have been substantially smaller during the period 13–5 ka than at the present day.

Estimates of the total Neoglacial volume change, $\Delta V \equiv V_{\max} - V_{\min}$, must be made in a fairly crude manner. These estimates are given in Section 6. A preliminary study found that the assumption of equivolume changes for each Neoglacial period was su cient for parametrizing the load, at least as it a ected the prediction of present-day isostatic uplift rates.

2.3 Last Glacial Maximum (LGM)

During the past 100 000 years, glaciation of the Andes south of 36°S involved at least three separate maxima (Llanquihue Glaciations I, II and III) (Porter 1981; Clapperton & Sugden 1988; Rabassa & Clapperton 1990; Clapperton *et al.* 1995). During a period when the Northern Hemispheric ice sheets were in rapid collapse (15–14 ka), Patagonian glacier advance ceases and subsequent retreat occurred rapidly, with the region being substantially deglaciating by 13 ka (Rabassa & Clapperton 1990). For load modelling purposes (see Figs 3 and 4) we assume the volume changes and timing of late Pleistocene Patagonian deglaciation that are given by Tushingham & Peltier (1991) in model ICE-3G, in spite of its relatively early completion of retreat at 15 ka. Inclusion of an 11–10 ka readvance has a negligible contribution to the present-day crustal motion signature, as has the inclusion of ocean loading. The total volume of ice lost during deglaciation from LGM,

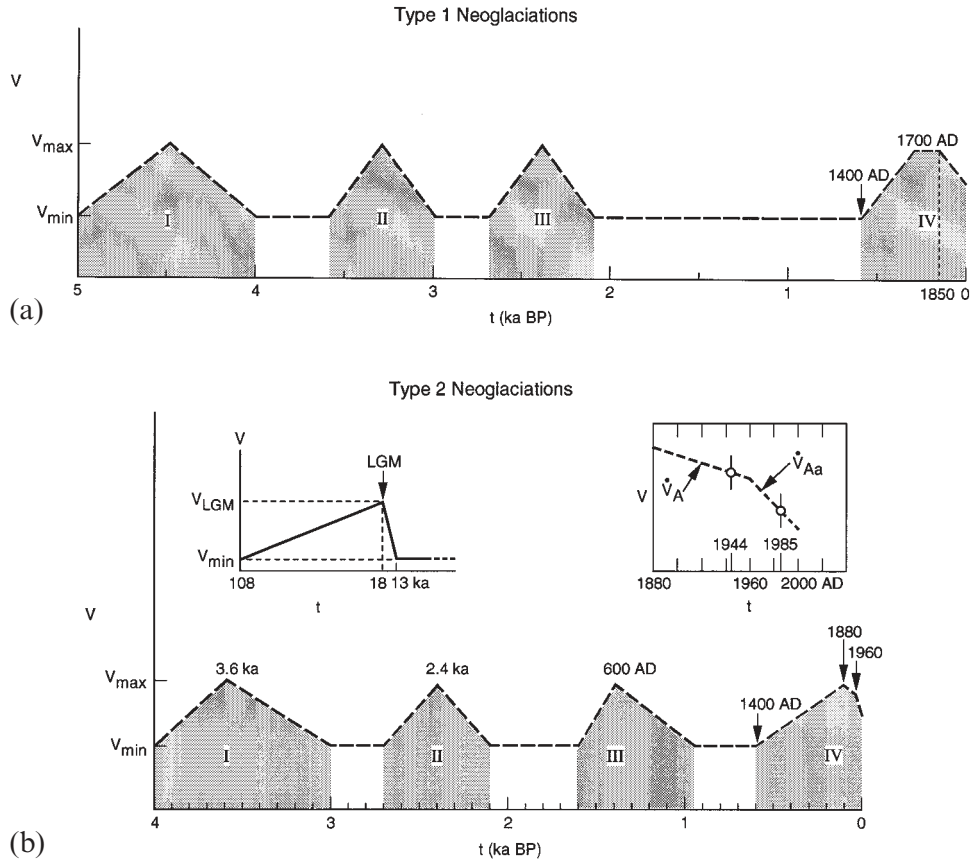

Figure 2. Two chronologies assumed for the mid- and late Holocene retreats and advances. Some of the main di erences between Neoglaciation scenarios 1 and 2 (frames a and b, respectively) are as follows. (1) Type 1 includes an early advance (phase I) beginning at 5 and ending at 4 kyr BP, a period of sustained minimal glaciation between 2.1 and 0.6 kyr BP and a 150-year-long maximal glacial volume sustained during the years 1700 to 1850 AD. The second, third and fourth (II, III and IV, respectively) phases coincide with the three Neoglacial chronologies adopted by Mercer (1970). (2) Type 2 scenarios have Neoglacial oscillations beginning at 4 kyr BP, include a Neoglacial initiated at 400 AD and a linear build-up of volume during the LIA (phase IV) from 1400 to 1880 AD. Type 2 chronology coincides with a recent estimate of Aniya (1995) for the Tyndall and Upsala glaciers. Type 1 assumes a constant volumetric rate $\dot{V}_A$ in accordance with the observations of Aniya *et al.* (1996, 1997), whereas Type 2 also considers a slow recession phase during 1880 to 1960 followed by an accelerated phase at rate $\dot{V}_{Aa}$ (at the minimum and maximum volumetric rates determined by Aniya *et al.* 1997.

as portrayed in ICE-3G, is $\Delta V_{LGM} \approx 1.8 \times 10^5$ km^3. Mid- and late Holocene oscillations represent a small fraction of the mass change associated with deglaciation from 21 to 13 ka. The Llanquihue moraine advances (Rabassa & Clapperton 1990) are more closely represented by the Neoglacial disc structure (see Figs 5 and 6) than by the larger ICE-3G discs (see Fig. A3), and the former structure is used in all computations reported here. Other computations were performed with the ICE-3G disc structure, but this had a negligible influence on the predictions of combined LGM plus Neoglacial present-day isostasy.

3 MOTIVATION FOR A SIMPLIFIED EARTH MODEL WITH COMPLEX LOAD PATTERN AND HISTORY

Over the past 30 years a series of global glacioisostatic models have been employed to explain the ^{14}C-dated palaeoshoreline record. Mantle viscosity structure plays a prominent role in such models, for it controls, to a significant extent, the timing, pattern and magnitude of postglacial isostatic land emergence and subsidence (e.g. Walcott 1970; Peltier 1976; Lambeck 1993). Mantle viscosity plays a vital role since the timescales for global deglaciation phenomena ($\approx 10^3$–10^4 yr) and viscous–gravitational relaxation ($\approx 10^2$–10^4 yr) overlap. Simple models of the viscously lagged isostatic response are useful when the underlying concern is over the spatial pattern, total hydrological mass and chronology of a region having a poorly constrained glacial history. By assuming the mantle structure to be known, ice load models may be sought by iteration with the goal of fitting local land emergence records. For example, using a simple parametrization of the viscous isostatic response, Broecker (1966) interpreted ^{14}C dated palaeoshorelines of proglacial lakes with the intent of deriving first-order constraints on ice sheet geometry during Laurentide advancement and retreat. One drawback of the latter approach is a lack of wavelength sensitivity in the exponential response times, and this is a severe limitation when the load has geometrical complexity.

Most simple models assumed by glaciogeomorphologists are in stark contrast to the sophisticated treatments developed for analysis of global postglacial shoreline data (e.g. Peltier 1974, 1976; Mitrovica & Peltier 1991; Lambeck 1993). In this paper we develop a semi-analytical approach that retains the essentials of Maxwell viscoelastic gravitational relaxation and apply this method to the retreats and advances of the Patagonian glacier fields during the late Holocene. The model and method o er a compromise between the sophisticated global spherical models and those that assume a single-mode, viscously lagged, postglacial response such as assumed by Broecker (1966). The model also o ers a more sophisticated approach than those models in current use for ice sheet modelling purposes (see a recent summary by Huybrechts 1992). Using this simple numerical tool we may span both the viscosity and the lithospheric thickness parameter space along with a spatially detailed and temporally varying ice load. The predicted uplift signature for Patagonia due to 20th century glacial recession is significant ($\dot{w} \geq 4$ mm yr^{-1}) over a quite plausible portion of the mantle viscosity and lithospheric thickness parameter space.

4 UPPER MANTLE RHEOLOGY AND LITHOSPHERIC THICKNESS

4.1 Laterally heterogeneous upper mantle and lithosphere

The e ective viscosity of the mantle, thickness of the lithospheric and elastic rigidity in most simple continuum mechanical models set the timescales for these gravity-driven isostatic responses (McConnell 1965; Walcott 1970; Peltier 1976). Using the global sea level record Peltier (1976), for example, has constrained spherically symmetric, radially varying, viscosity models of the mantle. Although such models provide a global average, Nakada & Lambeck (1991), Ivins & Sammis (1995), Kaufmann & Wolf (1996), Giunchi *et al.* (1997) and others have emphasized that lateral heterogeneity in the upper mantle probably exceeds one order of magnitude in viscosity and that regional estimates must account for the continental-scale tectonic environment. Models for sea level change and time-dependent shoreline evolution driven by the removal of glacial ice that covered northern Europe during glacial times (100–21 kyr BP) provide some estimate of both the viscosity and the lithospheric thickness beneath Fennoscandia. Recent modelling by Mitrovica (1996) indicates that the lithosphere beneath Fennoscandia is roughly 75–120 km thick and the upper-mantle viscosity is bounded between about 6.5 and 11.0×10^{20} Pa s. Another analysis of the northern European LGM and subsequent ice retreat (Lambeck 1993) determined that an optimum fit to relative sea level changes along the coast of the British Isles corresponds to an elastic lithospheric thickness of 65 km and an upper-mantle viscosity near 4–5×10^{20} Pa s. However, an even smaller upper-mantle viscosity (1–2×10^{20} Pa s) and thinner elastic lithosphere values (50 km) fit palaeoshoreline data along the eastern coast of Australia (Nakada & Lambeck 1989), and analyses of glacioisostatic rebound in Iceland, near an active oceanic spreading centre, indicate a regional upper-mantle viscosity lower than 1×10^{19} Pa s (Sigmundsson 1991). Modelled post-seismic (Matsu'ura & Iwasaki 1983) and glacio–hydroisostatic (Maeda *et al.* 1992) coastal tilting and rebound in the island arc setting of Japan indicate that the sublithospheric viscosity is also fairly low, in the range 2×10^{19}–2×10^{20} Pa s. It is important to note that the crustal deformation decay timescales set by such estimates of viscosity and lithospheric thickness for this island arc environment are similar to those corresponding to well-documented centennial and millennial scale climate changes such as the LIA.

4.2 Patagonian tectonic framework

The Miocene and Plio-Pleistocene magmatic and tectonic history of Patagonia is characterized by the northward migration of the Chile Triple Junction and the progressive subduction of active ridge segments (Candie & Leslie 1986). A substantial 'slab window' has developed beneath Patagonia due to the oblique angle of this subduction (Gorring *et al.* 1997). The implied thermorheologic weakening associated with both ridge subduction (Hsui 1981) and slab window evolution (Thorkelson 1996; Goes *et al.* 1997) suggest that the mechanical strength properties of the Patagonian lithosphere and upper mantle are more analogous to an island arc setting (Stern & Kilian 1996) than to a continental shield environment.

In this paper we present the results of a numerical modelling study that treats the lithosphere as an elastic layer and the upper mantle as a homogeneous Maxwell viscoelastic half-space (Fig. 3). Both regions are hydrostatically pre-stressed. The governing equations are essentially the same as given by Peltier (1976) except that the geometry is simplified to a cylindrical coordinate frame and material compressibility, along with certain self-gravitational terms, are ignored. A recent study by Johnston *et al.* (1997) has shown that finite compressibility is an important property for computing horizontal displacements. However, its influence on the vertical field is relatively minor (Wolf 1985b). A rather complete discussion of the system of equations was given by Wolf (1985a) and the numerical procedures adopted here are similar to this study. An extensive investigation of the icefield load history and its influence on the prediction of present-day vertical motion is undertaken. We now give a complete account of the simple theory for solid Earth deformation.

5 THEORY

5.1 Equations of motion and reduction to an ODE form

Within a layer of constant density, ρ, the perturbation equations for the displacement field, $\mathbf{u}$, and stress tensor, τ, are

$$\nabla\cdot\tau+\rho g\nabla(\mathbf{u}\cdot\mathbf{k})=0\,, \tag{1}$$

where g is gravity acting parallel to the unit vector $\mathbf{k}$ of the positive (downward-directed) z-axis in a cylindrical coordinate system (r, z, θ). For axisymmetric loading and assuming lateral homogeneity, the Eulerian displacement is

$$\mathbf{u}=u(r,z,t)\mathbf{r}+w(r,z,t)\mathbf{k}\,, \tag{2}$$

with $\mathbf{r}$ the unit vector in the radial direction. If the lithosphere and mantle are elastic, then time, t, does not enter as an independent variable. For isotropic elasticity,

$$\tau=\left(\kappa^{\mathrm{e}}-\frac{2}{3}\mu^{\mathrm{e}}\right)\mathrm{tr}\,\{\varepsilon\}\boldsymbol{I}+2\mu^{\mathrm{e}}\varepsilon\,, \tag{3}$$

where $\mathrm{tr}\,\{\varepsilon\}$ is the trace of the deformation tensor, ε, $\boldsymbol{I}$ is the identity tensor, and κ^{e} and μ^{e} are the bulk and shear moduli, respectively. The r and z components of the equation of motion (1) are then

$$\frac{\partial\tau_{rr}}{\partial r}+\frac{\partial\tau_{rz}}{\partial z}+\frac{(\tau_{rr}-\tau_{\theta\theta})}{r}+\rho g\frac{\partial w}{\partial r}=0\,, \tag{4a}$$

$$\frac{\partial\tau_{rz}}{\partial r}+\frac{\partial\tau_{zz}}{\partial z}+\frac{\tau_{rz}}{r}+\rho g\frac{\partial w}{\partial z}=0\,. \tag{4b}$$

The stress–strain relations in cylindrical coordinates allow for some simplification of (4a). In particular,

$$\frac{\partial\tau_{rr}}{\partial r}+\frac{\partial\tau_{rz}}{\partial z}+\frac{(\tau_{rr}-\tau_{\theta\theta})}{r}=2\mu^{\mathrm{e}}(\varepsilon_{rr}-\varepsilon_{\theta\theta})+\left(\kappa^{\mathrm{e}}-\frac{2}{3}\mu^{\mathrm{e}}\right)\left[\frac{1}{r}\frac{\partial(ru)}{\partial r}+\frac{\partial w}{\partial z}\right], \tag{5}$$

where ε_{rr} and $\varepsilon_{\theta\theta}$ are strain components in cylindrical coordinates. Use of the latter strain components, stress–strain relations for τ_{zz} [see Jaeger 1969, pp. 61–62] and the following derived from (5):

$$\frac{\partial w}{\partial z}=\frac{2\mu^{\mathrm{e}}-3\kappa^{\mathrm{e}}}{4\mu^{\mathrm{e}}+3\kappa^{\mathrm{e}}}\frac{1}{r}\frac{\partial(ru)}{\partial r}+\frac{3}{4\mu^{\mathrm{e}}+3\kappa^{\mathrm{e}}}\tau_{zz}\,, \tag{6}$$

allows (4a) to be rewritten as

$$\frac{\partial\tau_{rz}}{\partial r}+\frac{3\kappa^{\mathrm{e}}-2\mu^{\mathrm{e}}}{4\mu^{\mathrm{e}}+3\kappa^{\mathrm{e}}}\frac{\partial\tau_{zz}}{\partial z}+\frac{4\mu^{\mathrm{e}}(3\kappa^{\mathrm{e}}+\mu^{\mathrm{e}})}{4\mu^{\mathrm{e}}+3\kappa^{\mathrm{e}}}\left(\frac{\partial^2}{\partial r^2}+\frac{1}{r}\frac{\partial}{\partial r}-\frac{1}{r^2}\right)u+\rho g\frac{\partial w}{\partial r}=0\,. \tag{7}$$

The first-order Hankel transform of (7) is defined by the integral operator

$$\hat{f}_1(k)\equiv H_1[f(r);k]\equiv\int_0^\infty rf(r)J_1(kr)\,dr\,, \tag{8}$$

where the operator notation H_1 follows that of Sneddon (1972). Using transformation (8) on (7) yields

$$\frac{\partial\hat{\tau}_{rz1}}{\partial z}-\frac{3\kappa^{\mathrm{e}}-2\mu^{\mathrm{e}}}{4\mu^{\mathrm{e}}+3\kappa^{\mathrm{e}}}k\hat{\tau}_{zz0}-\frac{4\mu^{\mathrm{e}}(3\kappa^{\mathrm{e}}+\mu^{\mathrm{e}})}{4\mu^{\mathrm{e}}+3\kappa^{\mathrm{e}}}k^2\hat{u}_1-\rho g\hat{w}_0=0\,. \tag{9}$$

In (9) the zeroth-order Hankel transform has been introduced, where

$$\hat{f}_0(k)\equiv H_0[f(r);k]\equiv\int_0^\infty rf(r)J_0(kr)\,dr\,, \tag{10}$$

with $J_0(kr)$ and $J_1(kr)$ are zeroth- and first-order Bessel functions, respectively. Dependent variables transformed by these two integral operators correspond to the notation of forms $\therefore_0$ and $\therefore_1$, respectively. Applying the operator (10) to (4b) yields

$$\frac{\partial\hat{\tau}_{zz0}}{\partial z}+k\hat{\tau}_{rz1}+\rho g\frac{\partial\hat{w}_0}{\partial z}=0\,. \tag{11}$$

Hankel transforms of derivative terms are provided by Sneddon (1972). The remaining development is restricted to the incompressible case for which $\kappa^{\mathrm{e}}\to\infty$. In this case the following holds:

$$\frac{1}{r}\frac{\partial(ru)}{\partial r}+\frac{\partial w}{\partial z}=0\,, \tag{12}$$

and this allows (9) to simplify to the form

$$\frac{\partial\hat{\tau}_{rz1}}{\partial z}-k\hat{\tau}_{zz0}-4\mu^{\mathrm{e}}k^2\hat{u}_1-\rho g\hat{w}_0=0\,. \tag{13}$$

The zeroth-order transform of (12),

$$\frac{\partial\hat{w}_0}{\partial z}+k\hat{u}_1=0\,, \tag{14}$$

and the first-order Hankel transform of the stress–strain relation for τ_{rz},

$$\frac{\partial\hat{u}_1}{\partial z}-k\hat{w}_0-\frac{1}{\mu^{\mathrm{e}}}\hat{\tau}_{rz1}=0\,, \tag{15}$$

with (11) and (12), provide a coupled system of ordinary di erential equations in the dependent variables $\hat{u}_1(z,k)$, $\hat{w}_0(z,k)$, $\hat{\tau}_{rz1}(z,k)$ and $\hat{\tau}_{zz0}(z,k)$. The system (11)–(14) is identical to that of Wolf (1985a).

5.2 Gravitational forces

A key element was retained by Wolf (1985a,b) in contrast to earlier treatments of the axisymmetric elastic half-space problem in a cylindrical coordinate system by Farrell (1972). In particular, the term in (1) involving gravity and vertical displacement arises from the advection of initial hydrostatic pre-stress (Vermeersen & Vlaar 1991). Its existence allows gravitational restoring forces to act at any density interface such as the interface between the Earth's rock crust and the atmosphere or ocean. In the elastic problem, wherein (11), (13), (14) and (15) represent the static equilibrium conditions, gravity may play a fairly minor role (Ward 1984). However, when solid-state creep processes become important as in the case of glacial timescales, a physical description of isostasy and its time evolution require this term. In e ect, the gravitational buoyancy term allows for restoration of isostatic equilibrium after either loading or unloading events have ceased. This fact was discussed in the viscoelastic analogue of the well-known Boussinesq solution for an impulsive load by Peltier (1974).

For the elastic equilibrium equations (11), (13), (14) and (15), Wolf (1985b) recognized that the form of the matrix di erential system was identical to that of Farrell (1972), provided the stress variable $\hat{\tau}_{zz0}$ is modified to

$$\delta\hat{\tau}_{zz0} \equiv \hat{\tau}_{zz0} + \rho g \hat{w}_0 . \tag{16}$$

5.3 Viscoelastic solution for the *i*th layer

The correspondence principle of linear viscoelasticity allows the solution to be recovered from that of the elastic equations. This requires Laplace transformation to the variable s, and replacement of μ^e by $\mu(s)$ in the equilibrium equations. Henceforth, we assume the viscoelastic system with solution for the ith homogeneous layer:

$$_i\hat{u}_1(z, s, k) = -A_i\, e^{kz} + B_i\, e^{-kz} + kzC_i\, e^{kz} + kzD_i\, e^{-kz}, \tag{17a}$$

$$_i\hat{w}_0(z, s, k) = A_i\, e^{kz} + B_i\, e^{-kz} - (kz-1)C_i\, e^{kz} + (kz+1)D_i\, e^{-kz}, \tag{17b}$$

$$_i\hat{\tau}_{rz1}(z, s, k) = 2k\,{}_i\mu(s)[-A_i\, e^{kz} - B_i\, e^{-kz} + kzC_i\, e^{kz} - kzD_i\, e^{-kz}], \tag{17c}$$

$$_i\delta\hat{\tau}_{zz0}(z, s, k) = 2k\,{}_i\mu(s)[A_i\, e^{kz} - B_i\, e^{-kz} - (kz-1)C_i\, e^{kz} - (kz+1)D_i\, e^{-kz}]. \tag{17d}$$

The equivalent of (17) is given by Wolf (1985a), although his eqs (2a) and (2b) contain some typographical errors.

5.4 Boundary conditions and solution for a two-layer system

Whilst solutions (17a)–(17d) are appropriate for an N-layered half-space, we now use these to construct a model that describes the surface deformation of a two-layered system. The top layer corresponds to $i = 1$ and the half-space to $i = 2$. The surface of the top layer is loaded by a finite stress load, q, that represents the downward-directed force on the solid Earth at the base of an ice sheet. This force is balanced by the finite material strength of the crust, so that

$$_1\hat{\tau}_{zz0}(0, s, k) = -\hat{q}_0(s, k), \tag{18a}$$

where the load is assumed axisymmetric and $\hat{q}_0$ now is assumed to be in both the Laplace and the zeroth-order Hankel transform space, as indicated by the dependences upon s and k in (18). The ice sheet will be assumed to cause negligible transverse stresses, hence

$$_1\hat{\tau}_{rz1}(0, s, k) = 0 . \tag{18b}$$

Together, (18a) and (18b) represent the required boundary conditions at the ice–rock interface. Note, however, that (18a) is not expressed in terms of our dependent variables of the solution (17a)–(17d). Both of the cylindrical stress components $\tau_{r\theta}$ and $\tau_{z\theta}$ vanish everywhere in the space due to the assumed axisymmetry. It is convenient to reconsider the unmodified vertical stresses, $\hat{\tau}_{zz0}$, for completion of the solution. For a two-layer system the complete solution in the transform domain is obtained by solving for the unknown constant coe cients A_1, B_1, C_1, D_1, A_2, B_2, C_2 and D_2. Conditions of finite behaviour as $z \to \infty$ demand that $A_2 = C_2 = 0$. The two stress conditions (18a) and (18b) can be used to eliminate two of the constants for the top-layer solution. Use of the modified vertical stresses (16) in (18a) is facilitated by the simplicity of $_1\hat{w}_0$ at $z = 0$, noting that

$$_1\hat{w}_0(0, s, k) = A_1 + B_1 + C_1 + D_1 . \tag{19}$$

Additionally, it is convenient to write the unmodified stress as

$$_1\hat{\tau}_{zz0} = A_1\phi_1\, e^{kz} - B_1\chi_1\, e^{-kz} + (1-kz)C_1\phi_1\, e^{kz} - (kz+1)D_1\chi_1\, e^{-kz}, \tag{20}$$

where

$$\chi_1 \equiv 2k\mu_1 + \rho_1 g \tag{21a}$$

and

$$\phi_1 \equiv 2k\mu_1 - \rho_1 g . \tag{21b}$$

Eq. (2) allows the stress continuity conditions to be readily applied at the interface, $z = h$, between the top layer and the half-space. The latter conditions are

$$_1\hat{\tau}_{zz0} = {}_2\hat{\tau}_{zz0} \tag{22a}$$

and

$$_1\hat{\tau}_{rz1} = {}_2\hat{\tau}_{rz1}, \tag{22b}$$

and the displacement conditions at this interface are

$$_1\hat{w}_0 = {}_2\hat{w}_0, \tag{22c}$$

$$_1\hat{u}_1 = {}_2\hat{u}_1 . \tag{22d}$$

From the surface conditions (18a) and (18c) it can be easily shown that

$$D_1 = (\hat{q}_0 + 4k\mu_1 A_1 + \phi_1 C_1)/\chi_1, \tag{23a}$$

$$B_1 = -A_1, \tag{23b}$$

and, consequently, the four conditions at $z = h$, (22a)–(22d) form a 4×4 linear system for the constants A_1, C_1, B_2 and D_2. Such a system can be solved analytically. Below we combine only those parts of such a solution that are required for obtaining the uplift/subsidence at the surface, $z = 0$.

5.5 Surface vertical displacement solution

Upon obtaining the solution for the linear system, the remaining constants, B_2, D_2, A_1 and C_1, are eliminated and a complete solution in z is obtained. The vertical displacement solution ${}_1\hat{w}_0$ takes the simple form

$$(2k\mu_1 + \rho_1 g)\,{}_1\hat{w}_0 = 4k\mu_1(A_1 + C_1) + \hat{q}_0, \tag{24}$$

where the sum $A_1 + C_1$ is

$$\begin{aligned}\frac{A_1 + C_1}{\hat{q}_0} = \Big[& 2k\mu_2^2\{2k[1 + \mathrm{e}^{4kh} + 2\,\mathrm{e}^{2kh}(1 + 2k^2h^2)]\mu_1 \\ & - g\rho_1(1 - \mathrm{e}^{4kh} + 4kh\,\mathrm{e}^{2kh})\} \\ & + \mu_2\{-8k^2(1 - \mathrm{e}^{kh})(1 + \mathrm{e}^{kh})(1 + \mathrm{e}^{2kh})\mu_1^2 \\ & + 2kg[(\rho_1 + \rho_2)(1 + \mathrm{e}^{4kh}) + 2(\rho_2 - \rho_1)\,\mathrm{e}^{2kh}(1 + 2k^2h^2)]\mu_1 \\ & - \rho_1 g^2(\rho_2 - \rho_1)(1 - \mathrm{e}^{4kh} + 4kh\,\mathrm{e}^{2kh})\} \\ & + 4k^2\mu_1^3(1 - \mathrm{e}^{2kh} - 2kh\,\mathrm{e}^{kh})(1 - \mathrm{e}^{2kh} + 2kh\,\mathrm{e}^{kh}) \\ & - 2kg\rho_2\mu_1^2(1 - \mathrm{e}^{4kh} - 4kh\,\mathrm{e}^{2kh}) \\ & + g^2\rho_1(\rho_2 - \rho_1)\mu_1(1 - \mathrm{e}^{kh})^2(1 + \mathrm{e}^{kh})^2\Big]^{-1} \\ & \times \Big[-2k\mu_2^2\{1 + \mathrm{e}^{2kh}[1 + 2kh(1 + kh)]\} \\ & + \mu_2\{4k\mu_1 - g(\rho_2 - \rho_1)(1 + \mathrm{e}^{2kh}[1 + 2kh(1 + kh)])\} \\ & + \mu_1^2\{2k[(\mathrm{e}^{2kh} - 1) + 2kh\,\mathrm{e}^{2kh}(1 + kh)]\} \\ & + \mu_1 g(\rho_2 - \rho_1)[1 - \mathrm{e}^{2kh}(1 + 2kh)]\Big]. \end{aligned} \tag{25}$$

Note in (25) that the rheological parameters, μ_1 and μ_2, are isolated in each part of the expression. For either of the limits $\rho_2 \to \rho_1$, $\mu_2 \to \mu_1$ or $h \to 0$, corresponding to the half-space limit (Wolf 1985a), the correct limit $A_1 + C_1 \to 0$ is obtained.

5.6 Decay spectra γ_p

In eq. (25) both μ_1 and μ_2 might be considered viscoelastic due to fluid poroelastic and/or low-temperature creep in the crustal/lithospheric environment of layer 1 or due to high-temperature creep in the lower crust and/or mantle environment (layer 2). Although the upper crust may maintain a finite short-term viscoelasticity (Ivins 1996), a long-term, high-temperature creep deformation in layer 2 (half-space) dominates the total strain field associated with centennial and millennial timescale isostatic responses due to hydrological and sedimentary depositional transport. Our assumption is that the rheologies of regions 1 and 2 shown in Fig. 3 correspond to a constant elastic rigidity,

$$\mu_1 = \mu_1^{\mathrm{e}}, \tag{26a}$$

for the surface layer, and to a Maxwell material,

$$\mu_2 = \frac{\tau_{\mathrm{MX}} s}{1 + \tau_{\mathrm{MX}} s}\mu_2^{\mathrm{e}}, \tag{26b}$$

for the half-space. Here μ_1^{e} and μ_2^{e} correspond to the instantaneous elastic shear moduli. Eq. (26b) introduces τ_{MX}, the Maxwell time, equal to the ratio of long-term e ective viscosity η to short-term elastic modulus μ_2^{e}. The latter represents the 1/e-folding time for the transition to viscous-creep dominated deformation. Eq. (25), coupled with the simple material parameters of (26a) and (26b), a ords an extremely straightforward computation of analytic decay times. Expressions for the two decay times of the two-layer incompressible deformation are given in Tables 1 and 2. These free-decay eigenvalues, γ_p, are recovered from the inverse Laplace transform of eq. (24). Fig. A1 shows the inverse decay times, γ_p, as a function of Hankel wavenumber k assuming a 100 km thick elastic layer and a half-space viscosity of $\eta = 0.75 \times 10^{21}$ Pa s.

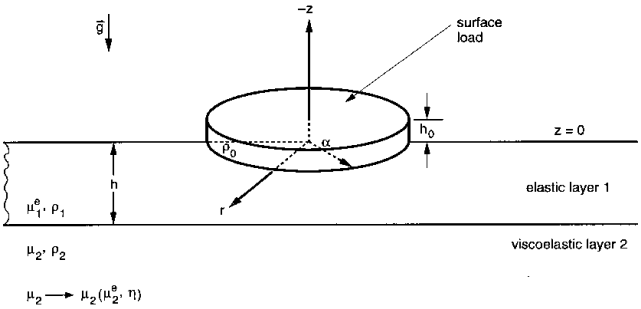

Figure 3. Basic model parameters for Earth structure and square-edged cylindrical disc load. The coordinate frame, with w positive downwards (see eq. 2), corresponds to the boundary value problem solution in Section 5. All deflections of the vertical described in Figs 5–A3, however, follow a standard convention, with uplift positive and subsidence negative.

5.7 Laplace transform inversion $\mathbf{L}^{-1}$

Analytic expressions for the time-dependent vertical displacement can be found in the Hankel transform domain. Let

Table 1. Terms forming γ_p and ξ_p.

n	$\hat{a}_n$
0	$4\frac{\mu_1^{\mathrm{e}}}{\mu_2^{\mathrm{e}}}k'^2[1 + \mathrm{e}^{4k'} + 2\,\mathrm{e}^{2k'}(1 + 2k'^2)]$
1	$2\rho_1\frac{gh}{\mu_2^{\mathrm{e}}}k'(1 - \mathrm{e}^{4k'} + 4k'\,\mathrm{e}^{2k'})$
2	$8\left(\frac{\mu_1^{\mathrm{e}}}{\mu_2^{\mathrm{e}}}k'\right)^2(-1 + \mathrm{e}^{k'})(1 + \mathrm{e}^{k'})(1 + \mathrm{e}^{2k'})$
3	$2k'\frac{gh}{\mu_2^{\mathrm{e}}}\frac{\mu_1^{\mathrm{e}}}{\mu_2^{\mathrm{e}}}[(\rho_1 + \rho_2)(1 + \mathrm{e}^{4k'}) + 2(\rho_2 - \rho_1)\,\mathrm{e}^{2k'}(1 + 2k'^2)]$
4	$\left(\frac{gh}{\mu_2^{\mathrm{e}}}\right)^2\rho_1(\rho_2 - \rho_1)(1 - \mathrm{e}^{4k'} + 4k'\,\mathrm{e}^{2k'})$
5	$4k'^2\left(\frac{\mu_1^{\mathrm{e}}}{\mu_2^{\mathrm{e}}}\right)^3(1 - \mathrm{e}^{2k'} - 2k'\,\mathrm{e}^{k'})(1 - \mathrm{e}^{2k'} + 2\,\mathrm{e}^{k'}k')$
6	$2k'\left(\frac{\mu_1^{\mathrm{e}}}{\mu_2^{\mathrm{e}}}\right)^2(1 - \mathrm{e}^{4k'} - 4\,\mathrm{e}^{2k'}k')\frac{gh}{\mu_2^{\mathrm{e}}}\rho_2$
7	$\frac{\mu_1^{\mathrm{e}}}{\mu_2^{\mathrm{e}}}\left[\frac{gh}{\mu_2^{\mathrm{e}}}(1 - \mathrm{e}^{k'})(1 + \mathrm{e}^{k'})\right]^2\rho_1(\rho_2 - \rho_1)$
8	$-2k'\{1 + \mathrm{e}^{2k'}[1 + 2k'(1 + k')]\}$
9	$4k'\frac{\mu_1^{\mathrm{e}}}{\mu_2^{\mathrm{e}}} - \frac{gh}{\mu_2^{\mathrm{e}}}(\rho_2 - \rho_1)\{1 + \mathrm{e}^{2k'}[1 + 2k'(1 + k')]\}$
10	$-2k'\left(\frac{\mu_1^{\mathrm{e}}}{\mu_2^{\mathrm{e}}}\right)^2[1 - \mathrm{e}^{2k'} - 2k'\,\mathrm{e}^{2k'}(1 + k')]$
11	$\frac{gh}{\mu_2^{\mathrm{e}}}\frac{\mu_1^{\mathrm{e}}}{\mu_2^{\mathrm{e}}}(\rho_2 - \rho_1)[1 - \mathrm{e}^{2k'}(1 + 2k')]$

Table 2. Dimensionless free modes $p = 1$ and $p = 2$.

$\hat{\beta} = \hat{a}_0 - \hat{a}_1 + \hat{a}_2 + \hat{a}_3 - \hat{a}_4 + \hat{a}_5 - \hat{a}_6 + \hat{a}_7$
$\hat{\beta}a_0 = \hat{a}_{10} + \hat{a}_{11}$
$\hat{\beta}a_1 = 2(\hat{a}_{10} + \hat{a}_{11}) + \hat{a}_9$
$\hat{\beta}a_2 = \hat{a}_8 + \hat{a}_9 + \hat{a}_{10} + \hat{a}_{11}$
$\hat{\beta}b_0 = \hat{a}_5 - \hat{a}_6 + \hat{a}_7$
$\hat{\beta}b_1 = \hat{a}_2 + \hat{a}_3 - \hat{a}_4 + 2(\hat{a}_5 - \hat{a}_6 + \hat{a}_7)$

Inverse decay time

$$\gamma'_p = \frac{b_1 \pm \sqrt{b_1^2 - 4b_0}}{2}$$

Amplitude factors

$$\xi'_p = \frac{(-1)^p}{\gamma'_2 - \gamma'_1}[\gamma'_p(a_1 - a_2\gamma'_p) - a_0]$$

$\hat{B}(k, s) \equiv (A_1 + C_1)/\hat{q}_0$ in (24) and, from (25) this can be written as

$$\hat{B}(k, s) = (a_2 s^2 + a_1 s + a_0)/(s^2 + b_1 s + b_0). \tag{27}$$

The inverse Laplace transform is found readily as

$$\mathbf{L}^{-1}\hat{B}(k, s) = \sum_{p=1}^{2} \frac{(-1)^p}{\gamma_2 - \gamma_1} \mathrm{e}^{-\gamma_p t}[\gamma_p(a_1 - a_2\gamma_p) - a_0] + a_2\delta(t), \tag{28}$$

where $\delta(t)$ is the Dirac delta function. The analytic solutions for inverse relaxation times γ_p ($\gamma_p = \gamma'_p/\tau_{\mathrm{MX}}$) are given in terms of the Earth-structure-dependent coe cients a_0, a_1, a_2, b_0 and b_1 in Tables 1 and 2 with dimensional coe cients, as used in (27) and (28), rescaled by $h/\eta\tau_{\mathrm{MX}}$, h/η, h/μ_2^{e}, $1/\tau_{\mathrm{MX}}^2$ and $1/\tau_{\mathrm{MX}}$, respectively. A convolution with the load $\hat{q}_0$ requires use of the Faltung theorem such that

$$\mathbf{L}^{-1}\{\hat{B}(k, s)\hat{q}_0(k, s)\} = \int_0^t \hat{B}(k, t - \tau)\hat{q}_0(k, \tau)\, d\tau. \tag{29}$$

Separating the spatial and time dependences of the load so that

$$\hat{q}_0 = \hat{q}_0^*(k)\hat{q}_0^{**}(t), \tag{30a}$$

and letting the surface stress load part, $\hat{q}_0^{**}$, be approximated as piecewise continuous with J linear segments,

$$\hat{q}_{0j}^{**} = \bar{m}_j t + \bar{b}_j, \tag{30b}$$

where $\hat{q}_0^*$ is that part associated with the Hankel wavenumber of the load, k. Examples of the decomposition (30b) are shown in Fig. 4, wherein $\hat{q}_{0j}^{**} = \rho_{\mathrm{ice}} g h_{0j}$. The amplitude factors, ξ_p, for the free-decay solution are defined from (28) as given in Table 2 and ξ'_p rescaled with h/η. At the termination of the jth interval, the contribution to the convolution from the interval has the sample form

$$\hat{Q}_j(k, t) = \sum_{p=1}^{2} \frac{\bar{b}_j \xi_p}{\gamma_p}[\mathrm{e}^{\gamma_p(t_j - t)} - \mathrm{e}^{\gamma_p(t_{j-1} - t)}] - \frac{\bar{m}_j \xi_p}{\gamma_p^2}[(1 - \gamma_p t_j)\,\mathrm{e}^{\gamma_p(t_j - t)} - (1 - \gamma_p t_{j-1})\,\mathrm{e}^{\gamma_p(t_{j-1} - t)}]. \tag{31}$$

At the termination of J linearly evolving intervals, and for all $t > t_J$, where t_J is the end time of the final linear segment, the complete convolution is

$$\mathbf{L}^{-1}\{\hat{B}(k, s)\hat{q}_0^{**}(s)\} = \sum_{j=1}^{J} \hat{Q}_j(k, t), \tag{32}$$

wherein the Earth is initially unloaded and in hydrostatic–gravitational equilibrium with $\bar{b}_1 = t_0 = 0$. An example of a linear load height history is shown in Fig. 4. Note that the memory e ect of any jth interval is captured by the terms $\mathrm{e}^{\gamma_p(t_j - t)}$. For example, the most recently 'memorized' event has a 1/e-folding time proportional to the time elapsed from the last portion of load evolution between t_{J-1} and t_J. For loads, $\hat{q}_0$, that have finite evolution during the evaluation time t, the convolution (29) must include the last terms of (24) and (28). Employing the appropriate integral relations (Dirac 1958, p. 59) and modifying $\hat{Q}_j$ of (32) for the Jth interval, we obtain

$$\hat{Q}_J(k, t) = (a_2 + 1/4k\mu_1^{\mathrm{e}})(\bar{m}_J t + \bar{b}_J) + \sum_{p=1}^{2} \frac{\xi_p}{\gamma_p^2}\{\gamma_p\bar{b}_J + \bar{m}_J(t\gamma_p - 1) - [\gamma_p\bar{b}_J + \bar{m}_J(t_{J-1}\gamma_p - 1)]\,\mathrm{e}^{\gamma_p(t_{J-1} - t)}\}, \tag{33}$$

with $t_{J-1} \le t \le t_J$. The modified term is of importance for computing the partly viscoelastic and partly elastic rebound occurring beneath the basement rock of an ice sheet whose mass balance evolves up to and including the present day. Note the sensitivity to the slope of the linear load evolution, $\bar{m}_J$, for time derivatives of (33), which largely control the prediction of vertical rates at time t.

5.8 Hankel transform inversion $\mathbf{H}_0^{-1}$

The case of a cylindrical load with square edges centred at $r = 0$ with form

$$q^*(r) = \begin{cases} 0 & r > \alpha \\ 1/2 & r = \alpha \\ 1 & r < \alpha \end{cases} \tag{34a}$$

has the forward transform $\mathbf{H}_0$,

$$\mathbf{H}_0\{q^*(r)\} \equiv \hat{q}_0^*(k) = \frac{\alpha}{k} J_1(k\alpha). \tag{34b}$$

The case of an ellipsoidal cross-section has the form

$$q^*(r) = \begin{cases} 0 & r > \alpha \\ \sqrt{\alpha^2 - r^2} & r \le \alpha \end{cases} \tag{35a}$$

and has the forward transform $\mathbf{H}_0$,

$$\mathbf{H}_0\{q^*(r)\} \equiv \hat{q}_0^*(k) = \frac{\alpha}{k} j_1(k\alpha), \tag{35b}$$

where j_1 is the spherical Bessel function of the first kind, of order one (see Wolf 1984 and Farrell 1972, respectively). In order to obtain the complete solution for an individual cylindrical disc load that is of constant radius α and evolving in time with the approximation (30b), the inverse zeroth-order Hankel transform $\mathbf{H}_0^{-1}$ must be computed. From (24), (27) and (32), the vertical displacement history is then

$$w_0(r, t) = \int_0^\infty \frac{4k\mu_1^{\mathrm{e}}}{2k\mu_1^{\mathrm{e}} + \rho_1 g}\left[\sum_{j=1}^{J} \hat{Q}_j(k, t)\right] J_1(k\alpha)\frac{\alpha}{k} J_0(kr)k\, dk. \tag{36}$$

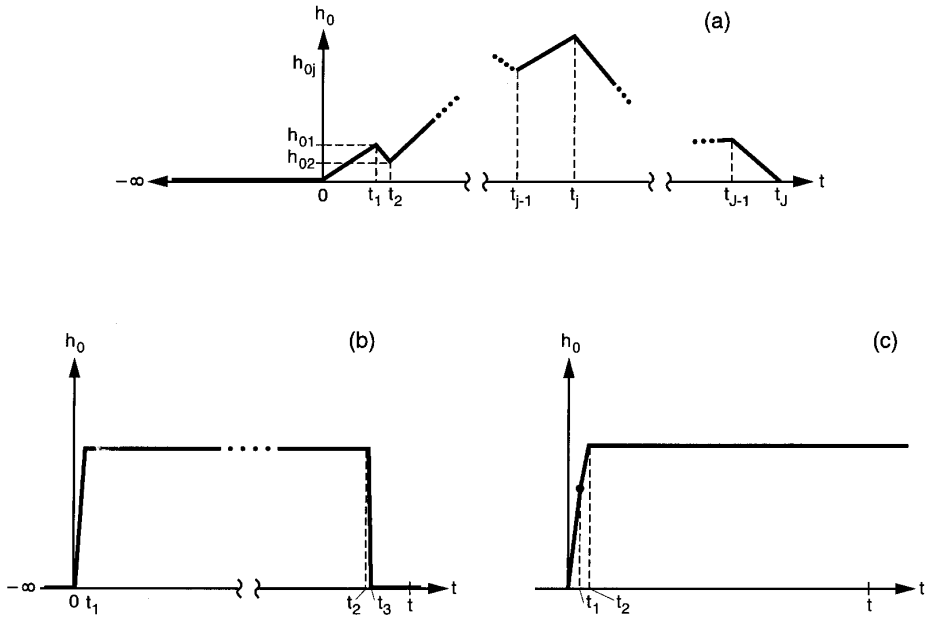

Figure 4. Model load height variation as a function of time. Case (a) shows an arbitrary history with a period of readvance. Cases (b) and (c) show approximate histories that can be used for benchmarking the theory and computer code by comparison with the results of Wolf (1985a). Cases (b) and (c) di er in that the model evaluation time t (see tick marks on time axis) in (c) must include the direct elastic e ect of the load, whereas in case (b) only viscoelastic e ects are present.

In practice, eq. (36) must be solved numerically, and it is useful to consider the following sampling for k. First, consider the smallest wavenumber to be comparable to the radius of the Earth, R, or

$$k \approx \frac{1}{R}.$$

However, much of the power in the deformation field is concentrated near the wavenumbers associated with the surface load and elastic layer thickness (McConnell 1965; Wolf 1993). The highest wavenumbers sampled in the integral (36) must allow

$$k > \max\left\{\frac{1}{\alpha}, \frac{1}{h}\right\}.$$

Introducing dimensionless time- and length scales and integral wavenumber, n,

$$\begin{aligned} t' &= \tau_{MX}^{-1} t, \qquad w_0' = h^{-1} w_0, \\ k' &= hk = nhR^{-1}, \qquad \alpha' = h^{-1}\alpha \end{aligned} \tag{37}$$

facilitates practical computation and the integral solution. Additionally, all stresses are scaled such that $\tau_{ij} = \mu_2^e \tau_{ij}'$. For $h = 100$ km the range for k' is 1.57×10^{-2} ($n \approx 1$) to 32.0 ($n \approx 2048$). The high resolution is noteworthy as this is similar to a spherical harmonic model of degree and order 2048 (Wolf 1984). This sampling is capable of resolving horizontal structure of the uplift/subsidence field at 10′, or at a wavelength comparable to 20 km. Sampling of k' may be tailored to shorter wavelengths. For example, a calculation for $h = 50$ km may assume higher resolution with the same truncation at maximum k' by doubling the truncation parameter for n. All computations given in this paper assume Simpson's rule for the approximation to (36). Note that the vertical rates, $dw_0(r, t)/dt$, can be computed from the derivative, $d\hat{Q}/dt$, in (32).

6 MODELS OF PATAGONIAN HOLOCENE FLUCTUATION

6.1 Estimation of ΔV

The total volume change, ΔV, between times of maximum glacial advance and retreat can only be crudely estimated. The SPI and NPI cover about 1.3×10^4 and 0.42×10^4 km^2, respectively. Rates of volume change during the period 1944–1985 are available only for the SPI. Estimates based on the SPI observations (Aniya *et al.* 1996, 1997) are made for both the NPI and the smaller glacier system in the vicinity of the Magellan Strait. This strategy lowers the overall estimate of the total loading of the lithosphere in the Patagonian region.

Change in glacier area is readily deciphered from aerial photography and satellite imagery. By incorporating ground-based surveys and oblique aerial photography, Aniya *et al.* (1997) were able to estimate the volume loss due to thinning of the SPI at about 100–300 km^3 over a 41 year period spanning 1944 to 1985. An additional 40–80 km^3 of ablation was attributed to retreat of the glacial fronts. Observations of the rate of thickness change vary from extreme thinning at -11.1 m yr^{-1} to a thickening rate on the Moreno glacier of 2.7 m yr^{-1}. To obtain an estimate of the change over a Neoglacial advancement phase, we approximate the 48 SPI outlet glaciers as equivolume masses having a cross-sectional area given by the equilibrium profile for a 2-D glacier obeying Glen's flow law (Hutter 1983, p. 284). Truncating these idealized volumes with square edges, so that the longitudinal dimension is W, the volume of a single outlet glacier of flow law power index $n = 3$ is then

$$V = \frac{2}{3}\gamma^* \bar{D}\bar{W}\bar{L}, \tag{38}$$

where $\gamma^* \equiv \Gamma(3/8)\Gamma(7/4)/\Gamma(9/8) \approx 0.6006$. Here $\bar{L}$ is the half-

width along the cross-section, $\bar{D}$ is the maximum depth (along the central axis) and Γ is the Euler gamma function. Typical dated moraine deposits show that the LIA and earlier Holocene advances are about 1–2 km, or larger. A total volume estimate using $N_{\mathrm{SPI}} = 48$ plus $N_{\mathrm{NPI}} = 28$ for this glacier prototype yields 15 450 km^3, for $\bar{D} = 440$ m, $\bar{L} = 10$ km and $\bar{W} = 30$ km. Such a value is in rough accord with the inventories tabulated by Aniya *et al.* (1996). A more precise estimate is unnecessary, as it is the di erential Neoglacial ice volume that determines the load change. Taking the total di erential of (38),

$$dV \approx 1.54(N_{\mathrm{SPI}} + N_{\mathrm{NPI}})(d\bar{D}\bar{L}\bar{W} + d\bar{W}\bar{L}\bar{D} + d\bar{L}\bar{W}\bar{D}), \qquad (39)$$

and estimating the di erential values to be 0.17, 1.9 and 4.0 km for $d\bar{D}$, $d\bar{L}$ and $d\bar{W}$, respectively, roughly consistent with the advances mapped by Mercer (1970, 1976, 1982), Rabassa & Clapperton (1990) and Aniya (1995), gives $dV = 10\,964$ km^3. If these were positive (accumulation) changes it would correspond to a 3.4-fold increase in ice volume and a 0.028 m lowering of eustatic sea level.

In order to expedite the parameter study it will be assumed that the Neoglacial di erential volume for the entire Patagonian icefields, including that of the Cordillera Darwin, south of the Magellan Strait, is $\Delta V = 1.0 \times 10^4$ km^3. Similarly, for the rate sustained from 1944 to 1985 the same type of distribution is assumed. Consequently, an identical disc thinning rate, $\dot{h}_{0ji}$, is assumed for each member of the pattern of discs shown in Fig. 5 during each jth time interval. In terms of the ith disc load (Fig. 3), it is assumed that all advance and recession is approximated by a linear rate $\dot{h}_{0ji}$ with each radius α_i held constant (Fig. 4) for the entire duration of loading and unloading. The uniform rate of height change for the maximum and minimum estimates for SPI during 1944–1985 by Aniya *et al.* (1997), distributed over all discs shown in Fig. 5, are $\dot{h}_{0Ji} = -0.13$ and -0.36 m yr^{-1}, respectively. Such values are consistent with direct observations. The estimates of volume change rates and magnitudes for the Holocene fluctuation model assumed (Fig. 2) are consistent with the numerical studies of Hulton *et al.* (1994) and Naruse *et al.* (1995). The former study shows that a 25–50 m decrease in the equilibrium line altitude (ELA) has the potential to cause order 0.1–1 $\times 10^4$ km^3 increase in total icefield volume over timescales of several centuries. It is plausible that such lowering of the ELA could be achieved by an atmospheric temperature decrease of about 0.5 °C (Hulton *et al.* 1994).

6.2 Possible Patagonian lithosphere–mantle structure

In Section 4 we briefly discussed the possible mechanical strength properties that might be applicable to the southernmost Cordillera of Chile and Argentina. The main point is that Patagonia and its environs are quite unlike Fennoscandia and eastern Canada, and all tectonic indicators suggest a mechanically weaker lithosphere and mantle. Lithosphere and mantle properties that have been derived from Fennoscandian rebound, therefore, provide a probable upper bound for an estimate of both lithospheric thickness and e ective mantle viscosity. Mitrovica (1996) has recently reanalysed Fennoscandian rebound constraints on lithospheric thickness and upper-mantle viscosity and determined the following range of values:

$75 \le h \le 125$ km,

$0.65 \times 10^{21} \le \eta \le 1.1 \times 10^{21}$ Pa s.

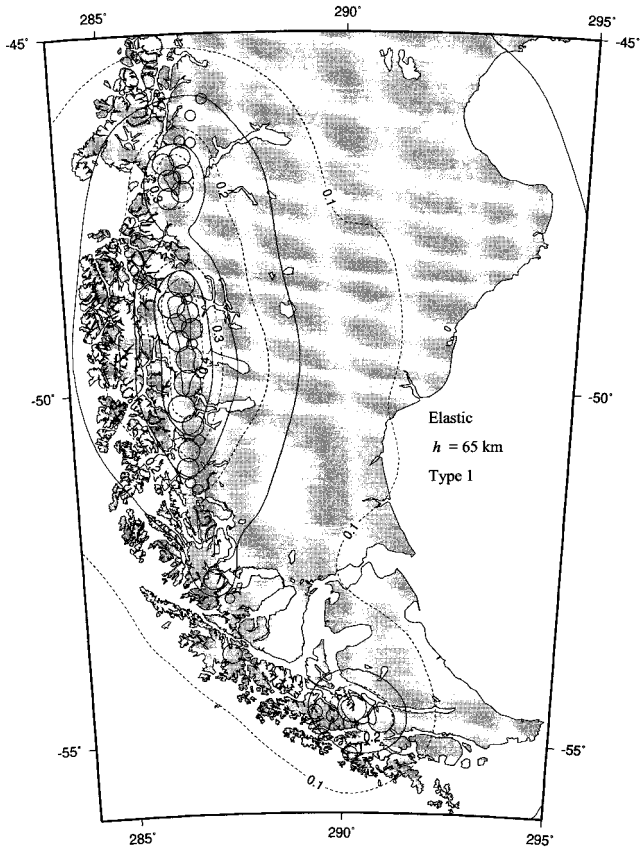

Figure 5. Vertical velocity in mm yr^{-1} due to elastic deformation in response to present-day ice recession. The elastic rigidities and densities are given in Table 3. Here the maximum glacial recession estimates from Aniya *et al.* (1997) for the period 1944/45 to 1985/86 are assumed to continue to the present day. The SPI loss rate estimate is applied to the entire icefield system as idealized by the circular (square-edged) discs as shown. This elastic response is implied in all computations. Here positive-valued contours indicate ongoing uplift.

We will refer to values in this range as 'Fennoscandian' structure. Another recent analysis of relative sea level history along the coastline of the UK by Lambeck (1993) has determined the following bound:

$60 \le h \le 75$ km,

$3 \times 10^{20} \le \eta \le 5 \times 10^{20}$ Pa s.

A lower viscosity seems to fit palaeoshoreline data from Australia (Nakada & Lambeck 1989) and bounds for this region are approximately

$50 \le h \le 100$ km,

$1 \times 10^{20} \le \eta \le 2 \times 10^{20}$ Pa s.

For the reasons summarized in Sections 4.1 and 4.2, and, in particular, the geologically recent creation of a 'slab-free window' (Gorring *et al.* 1997), each of these ranges probably overestimates the regional upper-mantle viscosity south of the Chile triple junction to varying degrees. Love and Rayleigh wave tomography indicate that the upper 100 km beneath Patagonia is similar to continental regions that presently experience tectonic extension and island arc volcanism (Montagner & Tanimoto 1991). Recent models of plume motion and the

relative fixity of hotspots indicate that the average upper-mantle viscosity beneath the lithosphere of the Pacific is 1.5×10^{20} Pa s or less (Steinberger & O'Connell 1998). Although the spectrum of possible lithospheric thicknesses and upper-mantle viscosities could be more extreme, we direct our study of mechanically weaker solid Earth structure to the parameter range

$$25 \leq h \leq 75 \text{ km},$$

$$5 \times 10^{18} \leq \eta \leq 1.0 \times 10^{20} \text{ Pa s}.$$

This realm is, essentially 'Basin and Range' in type.

The goal of the parameter study that follows is to find out how the predictions of present-day vertical isostatic rebound are influenced by the following unknowns: (1) variability in the Holocene icefield history (Fig. 2); (2) the rate of mass wastage of the icefields over the observation period 1944–1985, including post-1985 changes in that rate; and finally (3) the trade-o of vertical rate predictions with the mechanical strength of the lithosphere–mantle system.

6.3 Parameter study

For the purposes of the parameter study, it is assumed that the last Pleistocene ice age sets the viscoelastic gravitational conditions (amounting to a slight deviation from isostatic equilibrium by mid-Holocene time) for subsequent responses to ice volume oscillations during the late Holocene (≤ 5 ka). This era of glacial readvances in the region was termed 'Neoglacial' by Mercer (1970). The last of these advances may have a causal link to the lower worldwide temperatures during the LIA (e.g. Thompson *et al.* 1986). Subsequent retreat, known to be underway by 1880–1900 (Warren 1993), may possibly be linked to a global warming trend since 1850 (Jones *et al.* 1986). Recent studies of Antarctic deglaciation from the LGM by James & Ivins (1998) show that the relative youth of ice mass unloading there is quite important to the predicted present-day crustal motion. In contrast to the vast Antarctic ice sheet, constraints from the Holocene terminal moraines of the much smaller Patagonian icefields allows a parametrized study of isostatic response to quite young (0–5 kyr BP) glacial mass variations to be pursued.

6.3.1 Icefield change between 1944 and 1985 and to the present day: elastic rebound

Fig. 5 shows a contour map of the predicted present-day uplift rate given the volume change in the icefields over the 41-year observation period of Aniya *et al.* (1997), but distributed equally amongst the 36 discs shown and extended to the present day (AD 2000). The lithosphere–mantle structure assumed for the model in Fig. 5 is completely elastic and has the parameters given in Table 3 with $h = 65$ km. Here the elastic–gravitational rebound rate is directly proportional to $\dot{V}_A$, the volume rate from Aniya *et al.* (1997). The maximum rates of elastic uplift (Fig. 5) along the north–south axis of the icefields are in the range of 0.1–0.4 mm yr^{-1}.

6.3.2 Viscoelastic 'Fennoscandian' structure and Types 1 and 2 load histories

Figs 6(a)and (b) show the predicted present-day solid surface vertical displacement rate for Holocene histories of types 1 and 2 (Fig. 2). Here the lithosphere is assumed to be 65 km thick with the same rigidities and densities as in Fig. 5, except that the half-space (upper mantle) is Maxwell viscoelastic with a viscosity of $\eta = 6.5 \times 10^{20}$ Pa s. Our assumption of a 65 km thick lithosphere may be an underestimate for Fennoscandia, but this is somewhat irrelevant to our study, as the assumption of thicker lithospheres leads to nearly identical conclusions. Note from a comparison of Fig. 5 with Fig. 6 that larger rates are driven by the inclusion of a viscoelastic mantle and a Neoglacial history, and, more importantly, that the sign of the prediction reverses. This emphasizes the important aspect that viscoelasticity brings to interpreting present-day crustal uplift connected to observations of Holocene glacial variability and LIA growth and collapse. Viscoelasticity acts as a low-pass filter in time, so that it is the time-integrated ice mass changes and their e ect on isostasy that dominantly drive present-day uplift.

Table 3. Model mechanical parameters.

Symbol	Definition	Model value
ρ_{ice}	ice density	917.0 kg m^{-3}
ρ_1	lithospheric density	3380.0 kg m^{-3}
ρ_2	mantle (half-space) density	3590.1 kg m^{-3}
g	uniform gravity	9.832186 m s^{-2}
μ_1^e	lithospheric elastic rigidity	67 GPa
μ_2^e	mantle (half-space) elastic rigidity	145 GPa
η	mantle (half-space) viscosity	variable
h	lithospheric thickness	variable

A comparison of the cases shown in Figs 5 and 6 reveals that the details of the late Holocene history are likely to be more important than the purely elastic rebound. The latter is sustained only by present-day ice mass imbalances. This is demonstrated even though only a moderately weak earth structure model of 'Fennoscandian' type (Mitrovica 1996) has been assumed. Using the two types of glacial history (Fig. 2), we now explore the predictions associated with both 'Australian' and the much weaker 'Basin and Range' lithosphere–mantle structures.

6.3.3 'Australian' lithosphere–mantle structure

Assuming the same lithosphere thickness and glacial input parameters as are assumed for the computations shown in Fig. 6(b), Fig. 7 shows the predicted response with a viscosity that is consistent with an analysis of rebound along the coast of Australia (Nakada & Lambeck 1989). Assuming this lower viscosity, the predictions are large enough that the model input parameters might be testable using long-term GPS geodetic monitoring. It is useful to reference one site near the zone of maximum displacement rate (but outside the icefield) and another that is more than several load widths (comparable to the largest disc diameters in the load model) removed. The western reference site shown in Fig. 7 (the Chilean town of Villa O'Higgins) is near 48.5°S, 286.75°E (or 73.25°W). The eastern site is near 48.5°S, 289.0°E (the Argentine town of Tamal Aike). Villa O'Higgins (Fig. 7) sustains deformation that is consistent with the inner depression for all assumed earth structure models. For lithospheres thinner than about 50 km, Tamal Aike deforms as an outer peripheral bulge zone.

The subsidence at the present day that is predicted in Fig. 7 is quite unlike what we expect 120 years of deglaciation to

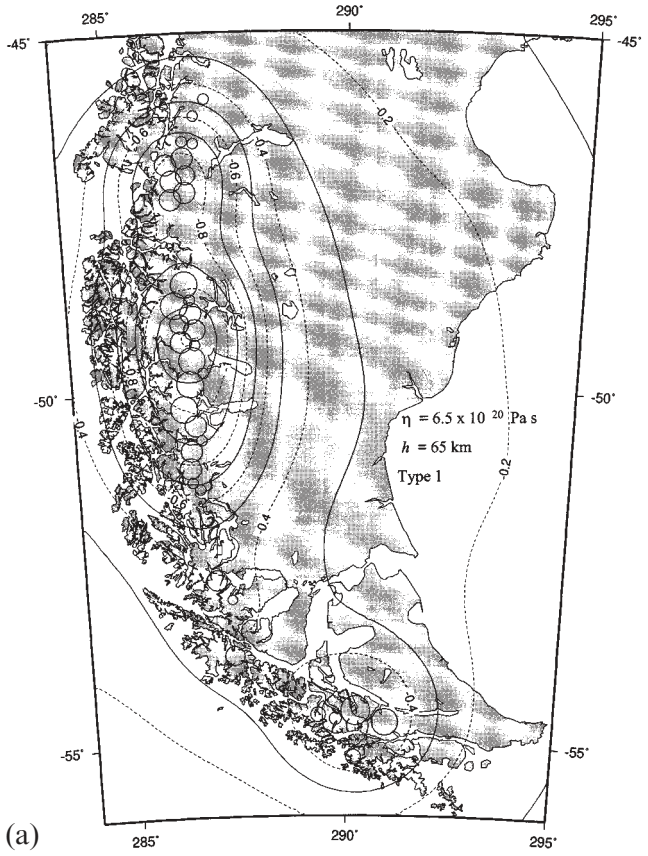

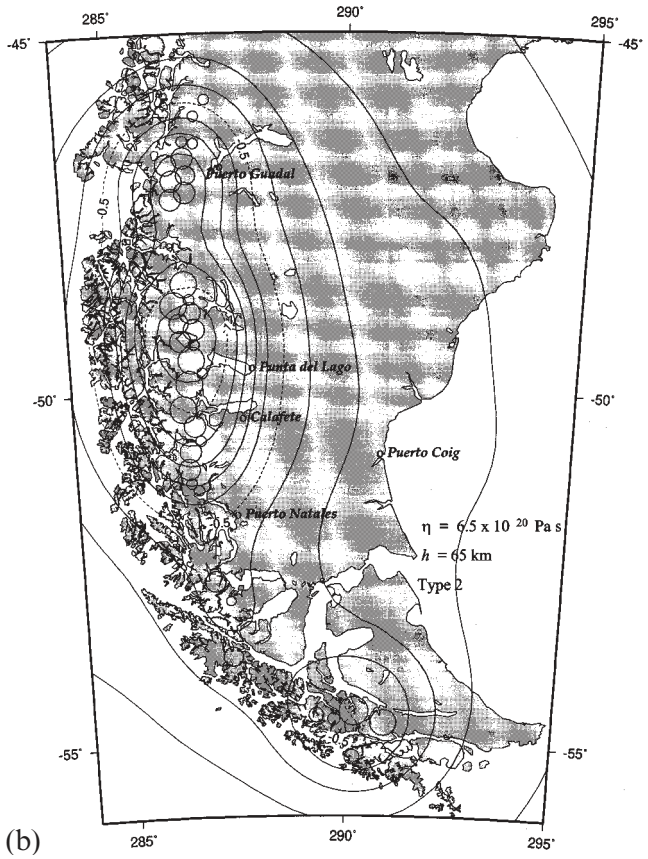

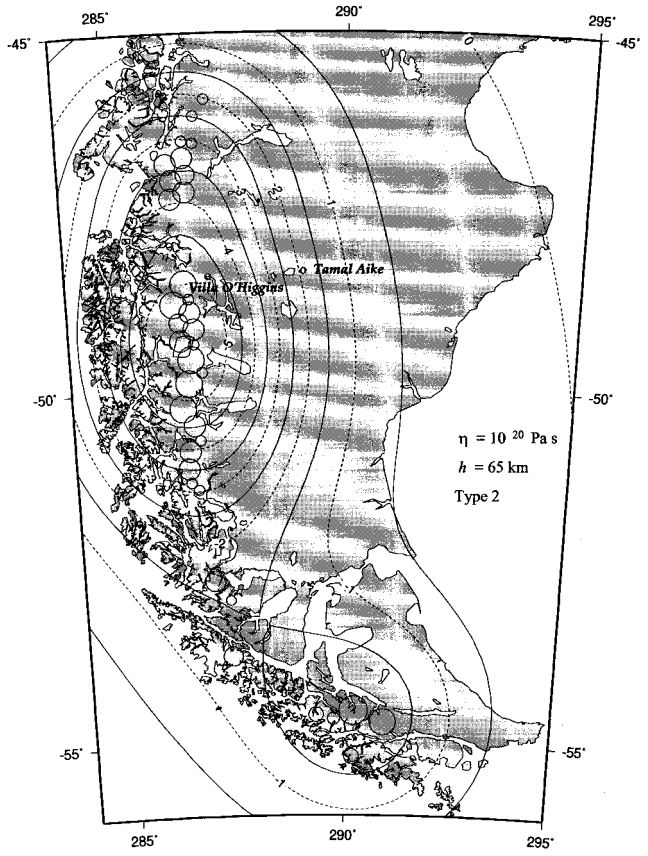

Figure 7. Predicted vertical velocity (mm yr^{-1}) for 'Type 2' load as in Fig. 6(a) with a smaller mantle viscosity ($\eta = 1.0 \times 10^{20}$ Pa s). All other earth structure and load parameters are identical to those assumed in Fig. 6. The assumed lithosphere/mantle structure is of 'Australian' type.

produce. What features of the model cause this? In order to understand the physical mechanisms that drive the present-day response it will be necessary to decompose the load history. Fig. 8 shows partitioned vertical rate predictions in which the pre-1400 AD Holocene (plus late Pleistocene LGM) are separated from post-1400 (LIA, or Neoglacial IV in Fig. 2) e ects. The separation demonstrates that the pre-1400 glacial load contributions lead to a rather classic style of isostasy: a load is emplaced at some time in the past and, after its removal, the depressed landscape uplifts. This type of response is shown at the left of each of the histograms of frames (a)–(c) in Fig. 8. Note that the Type 2 load will, in part, predict stronger pre-1400-induced present-day uplift rates than does Type 1 due to the presence of a more recent glacial oscillation (compare the two timings of Neoglacial III in Fig. 2). However, in a complete partitioning of the load (Fig. 9) it will be shown that

Figure 6. Predicted vertical velocity (mm yr^{-1}) for the two load histories of Fig. 2. Unlike Fig. 5, mantle viscoelastic deformation is accounted for. Frame (a) assumes a 'Type 1' load history and (b) assumes 'Type 2' with a uniform volumetric loss rate (as in Fig. 5) since AD 1850 and 1880 (see Figs 2a and b, respectively). Structure parameters are given in Table 3. Here negative-valued contours indicate the prediction of ongoing subsidence. Both frames have solid line contours at the 0.1 mm yr^{-1} levels. The assumed lithosphere/mantle structure is of 'Fennoscandian' type (see Section 6.2).

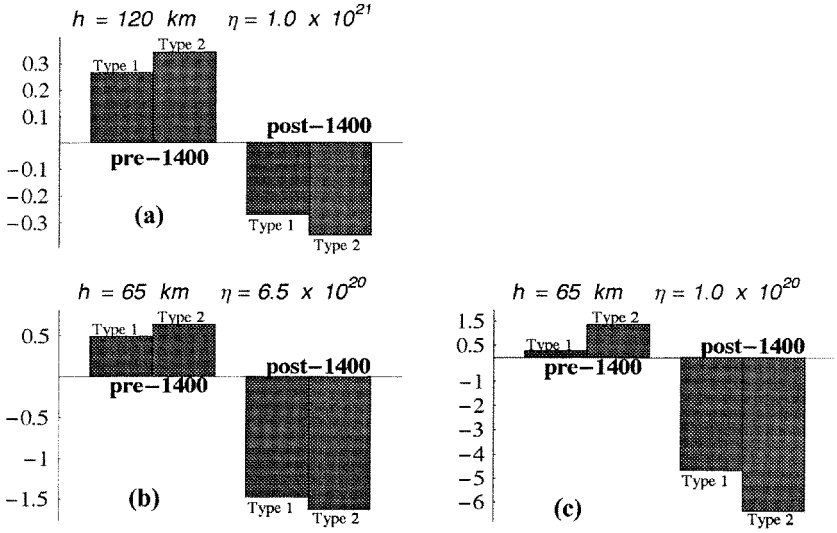

Figure 8. Partitioned vertical rate predictions (in mm yr^{-1}) at the Chilean town Villa O'Higgins (see Fig. 7). The partition assumes all three Neoglacials (I–III) plus LGM for pre-1400 AD load and only the LIA (IV) for post-1400 AD load.

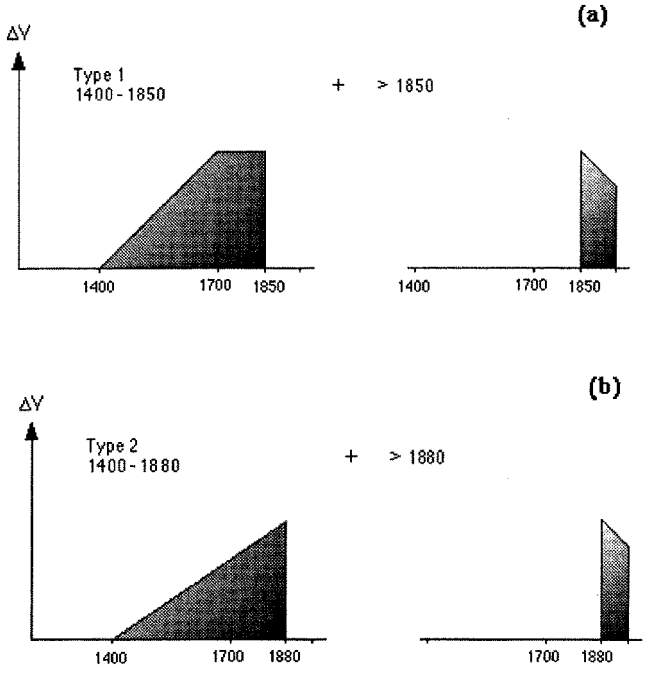

Figure 9. Refined partitioning of vertical rate responses for the LIA load (post-1400) alone. The partition is used for analysis of vertical rate predictions for viscosities $\eta \leq 1.0 \times 10^{20}$ Pa s. Note that the growth phase, when taken alone, should predict ongoing rebound (uplift), entirely analogous to classic near-field postglacial rebound due to deglaciation from late Pleistocene LGM.

the more robust present-day subsidence response of Type 2 is caused largely by the more recent termination of the post-1400 AD growth phase. We note that the computations for Fig. 8(a) assume a lithospheric thickness and an upper-mantle viscosity consistent with the global study of Tushingham & Peltier (1991). Frames (b) and (c) of Fig. 8 reveal the decreased role of the pre-1400 (pre-LIA) load as viscosity is decreased from 10^{21} Pa s. Here frames (b) and (c) correspond to the computational results shown in Figs 6 and 7.

6.3.4 *'Basin and Range' lithosphere–mantle structure*

As can be deduced from Fig. 8(c), a viscosity at or below 10^{20} Pa s responds primarily to the last mass oscillation of the icefields. Analysis in the lower viscosity range requires a decomposition of the LIA load. A refined partitioning of the post-1400 AD load is shown in Figs 9(a) and (b) for Types 1 and 2, respectively. The partitions produce predictions of uplift due to the portion at the left (growth phases) and subsidence due to the portion at the right (incomplete collapse phases).

Fig. 10 shows the LIA vertical rates predicted assuming the partitions shown in Fig. 9. The white line in the bar graph for Type 2 in the left of each frame indicates the response to the growth phase if it were terminated at the year AD 1850. This assumption for Type 2 allows for direct comparison to Type 1 growth in which the latter has a fixed load from AD 1700 to 1850 (see Figs 2 and 9). Note that an extension of the Type 2 growth phase by 30 years has a 20–25 per cent level contribution to the total 1400–1880 AD response partition (compare white line to the full bar graph). In each case a reduction by 30 years in the growth phase of Type 2 results in a weaker positive uplift. The map views that correspond to these cases are shown in Fig. 11.

A physical interpretation emerges from Fig. 10. Here the longer, or more robust, loading produces larger deviation from gravitational isostatic equilibrium. That larger disequilibrium, in turn, produces larger, and more recently initiated, isostatic uplift. However, in the shorter growth phase cases for Type 2 (white line), it is the Type 1 response, which is of smaller (negative) amplitude, that is added to form the total contribution. Type 2 loading, having no prolonged period of maximum glacial advancement, is less e cient than Type 1 loading (having achieved a maximum 150 years earlier than Type 2) in producing positive uplift at the present day. This conclusion is supported by each of the frames in Fig. 10.

Note that the partition in Fig. 10(a) shows a near-cancellation of the growth and collapse contributions. However, for the same earth structure and viscosity the prediction at the outer bulge position (Fig. 10b) shows stronger sensitivity to the

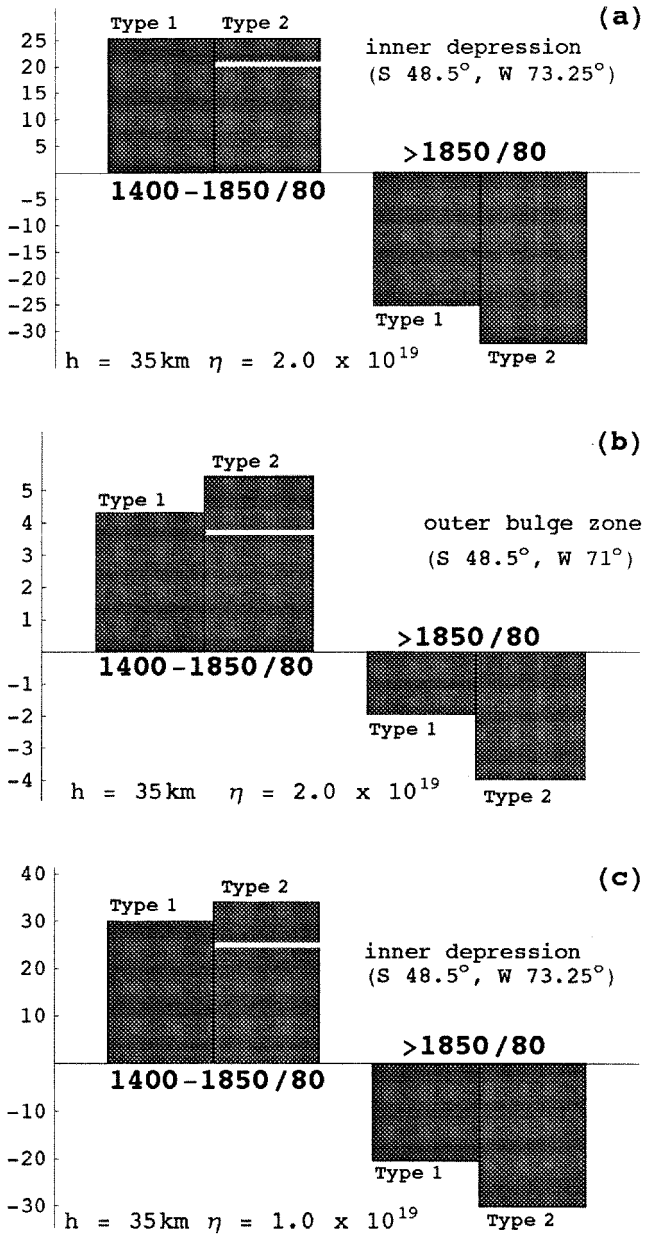

Figure 10. LIA vertical rates (in mm yr^{-1}) predicted assuming the partitions shown in Fig. 9. The white line in the bar graph for Type 2 in the left of each frame corresponds to a growth phase concluded at AD 1850, as in all Type 1 cases. The location termed 'inner depression' is identical to that assumed for Fig. 8. Note that the outer bulge zone and inner depression are analogous to 'zones 1 and 2' for postglacial isostatic emergent and collapsing forebulge coastal sites, respectively, as defined by Clark (1980). Map views of the total Neoglacial plus LGM predictions at the present day are shown in Fig. 11.

early part of the LIA. This is probably due to the fact that longer-wavelength components of the deformation field have a longer-term memory of the assumed 450 and 480 year growth phases than does the shorter-wavelength field. Frame (c) shows a lower-viscosity case that can be compared to frame (a). Note that in this lower-viscosity case (Fig. 10c), the total rebound from the AD 1400 to mid-19th century depression is stronger than in the higher-viscosity case (Fig. 10a). This greater e ciency is also allowed to act during the (incomplete) collapse phase. For example, the subsidence response to the collapse phase after 1850 in Type 1 is reduced by about 20 per cent over the higher-viscosity regime (compare right frames of Figs 10a and c), whilst the e ciency of the rebound rate component from pre-1850 is increased by 20 per cent (compare left frames of Figs 10a and c), and this produces a total positive rebound rate prediction for the present day for the lower viscosity ($\eta = 1.0 \times 10^{19}$ Pa s). This greater e ciency enhances the sensitivity to the volume reduction (unloading) during retreat from 1850 to the present day. The e ect is also seen in the Type 2 case.

6.3.5 Complex patterns of uplift and subsidence in the weak mechanical regime

Fig. 11 shows the total predicted vertical velocity for Type 1 (a and b) and Type 2 (c and d) for cases corresponding to the histograms of Fig. 10. The inner depression region, with predicted subsidence rates of -1.0 to 0 mm yr^{-1} in Fig. 11(a) are controlled almost entirely by the two LIA components (growth and collapse) as discussed in reference to Fig. 10. Note the broad zone of outer bulge uplift that is predicted at the level of 2–3 mm yr^{-1} in Fig. 11(a). With a factor of two reduction in viscosity (Fig. 10b), however, the inner depression zone uplifts at present day due to the enhanced e ciency of the rebound process (see the discussion in reference to Fig. 10). Here the rebound from the isostatic depression created during the first several hundred years of the LIA dominates over the (ablating) load imposition since the mid-19th century that continues to the present day.

Clearly, the higher-viscosity cases ($\eta > 2.0 \times 10^{19}$ Pa s) are relatively insensitive to ice mass changes over the past century and a half, but are quite sensitive to the fact that an LIA has e ectively produced a *net ice load* during the last 600 years. Hence, the higher-viscosity cases predict subsidence to be ongoing at the present day. The first explanation of this subtle physics involved in viscoelastic isostasy and the LIA was o ered by Wolf *et al.* (1997) in modelling the 20th century collapse of a major glacial system in Iceland. Here we have given some further explanation of this interesting sensitivity of geodetic observation to both the LIA and the mantle viscosity in Patagonia.

Both the 150 year evolutional hiatus at LIA maximum advancement and the earlier initiation of recession produces uplift in the case shown in Fig. 11(b) (Type 1 load) in comparison to the near-cancellation that is shown in Fig. 11(d) (Type 2 load) near the inner depression zone. Fig. 12 shows the vertical velocity predicted for $h = 25$ km. The viscosity is the same as in cases (b) and (d) of Fig. 11. Cases (a) and (b) assume load types 1 and 2, respectively. Type 1 (Fig. 12a) clearly shows the prediction of uplift as opposed to the subsidence (Fig. 12b) predicted by Type 2. An explanation of the di erences between these two predicted responses parallels that for Fig. 11 for $h = 35$ km at the same viscosity values. A comparison of Figs 12(a) and (b) reveals striking contrasts. Both a more e cient isostatic flow during loading for Type 1 history and the e ect of a 30 year lead in glacial recession dominate these di erences. When combined, the two load history e ects, at this lithospheric thickness value ($h = 25$ km), produce dramatically di erent predictions of uplift pattern. The di erences in prediction within the zone of central depression reach 14 mm yr^{-1}.

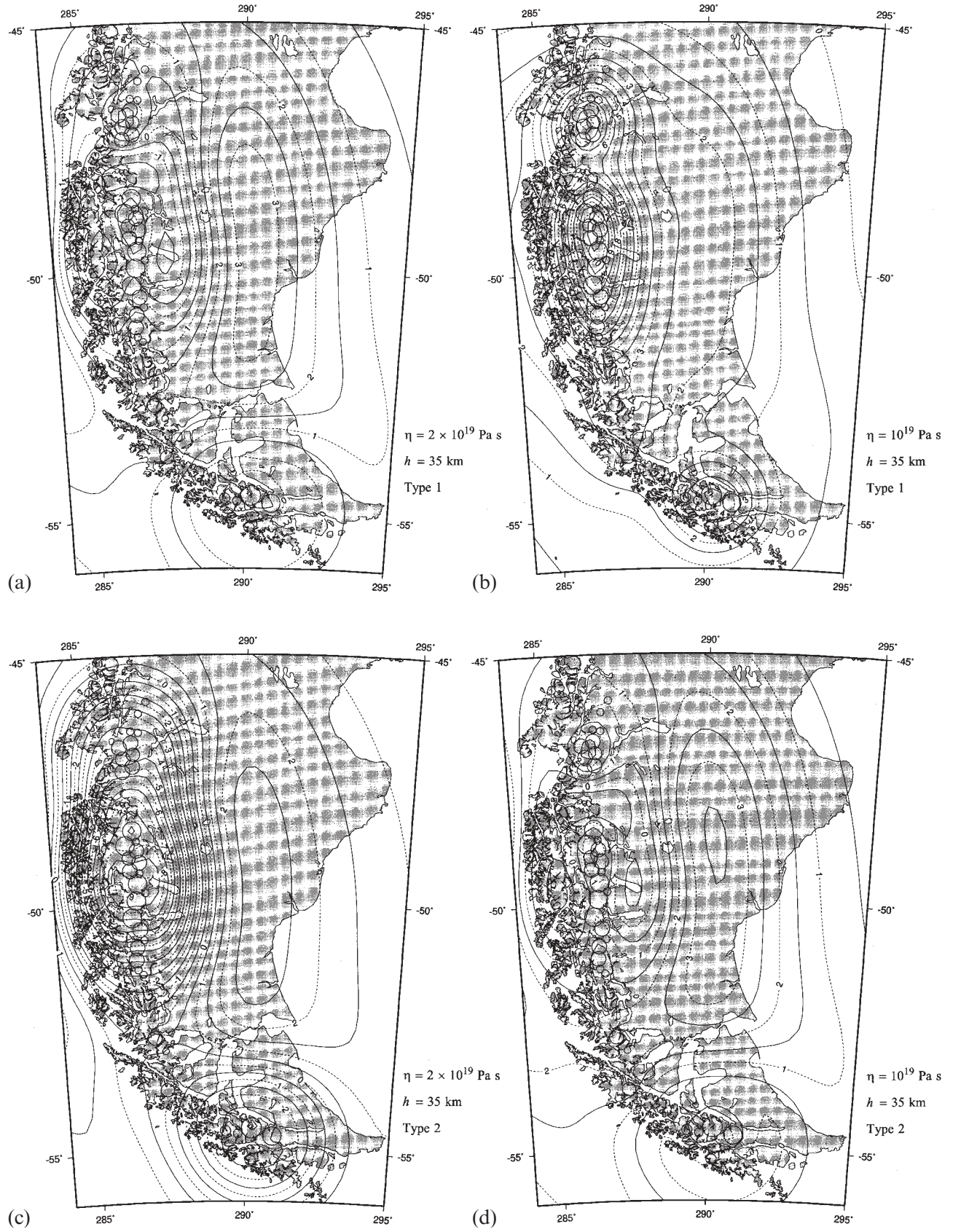

Figure 11. Predicted vertical velocity for Type 1 (a and b) and Type 2 (c and d) at two relatively low mantle viscosity values. Cases (a) and (c) assume $\eta = 2.0 \times 10^{19}$ Pa s whereas cases (b) and (d) assume $\eta = 1.0 \times 10^{19}$ Pa s with lithospheric thickness $h = 35$ km. The cases correspond to Fig. 10, but are shown in map view and show the total of all components on the predicted present-day rate. The assumed lithosphere/mantle structure is of 'Basin and Range' type.

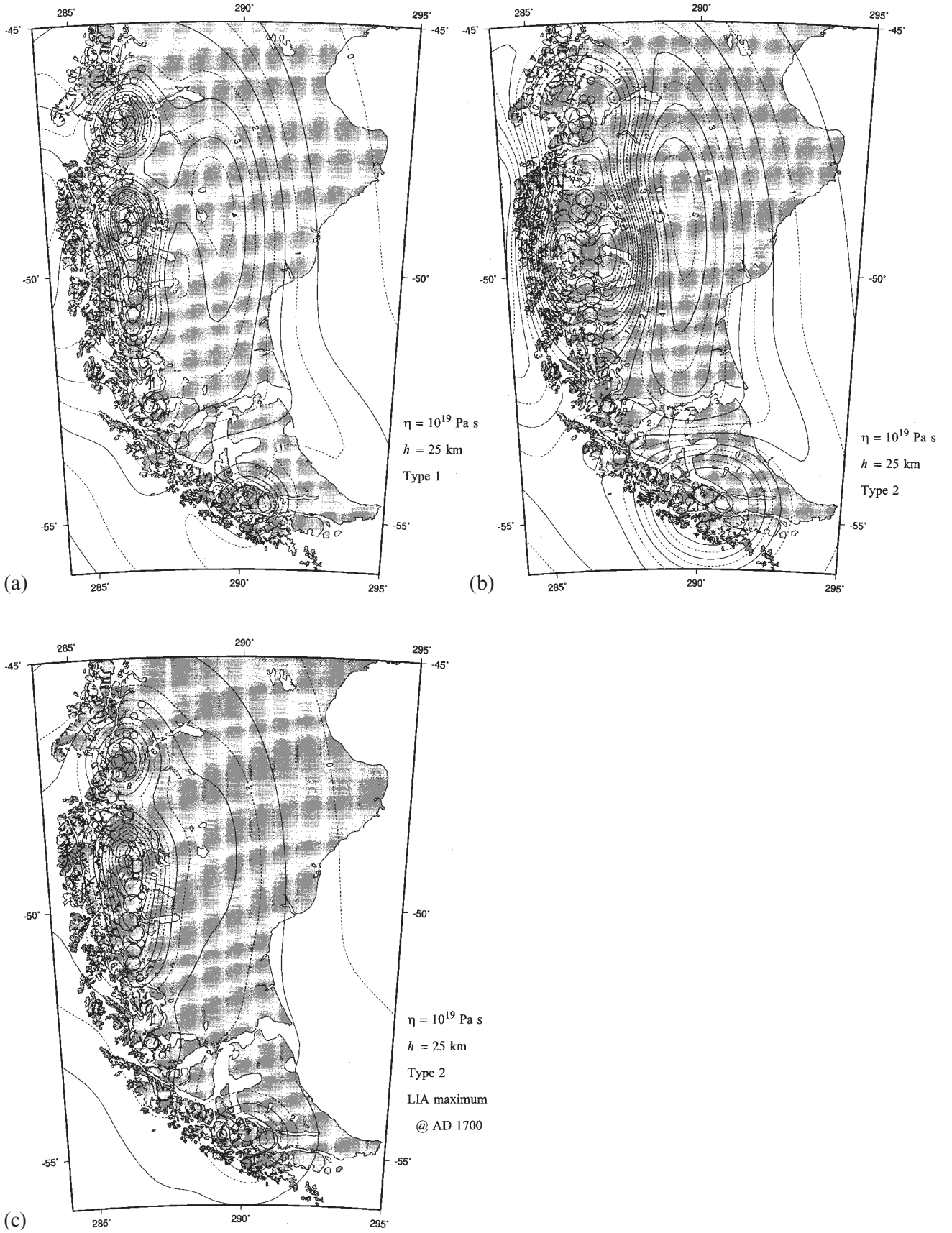

Figure 12. Predicted vertical velocity for $h = 25$ km. The viscosity is the same as in cases (b) and (d) of Fig. 11 ($\eta = 1.09 \times 10^{19}$ Pa s). Cases (a) and (b) assume load types 1 and 2, respectively. Case (c) assumes Type 2, but with the Neoglacial IV (see Fig. 2) maximum centred at the year AD 1700. Direct comparison of Fig. 12(a) with 11(b) reveals an enhanced outer bulge evolution in the thinner lithosphere case.

6.3.6 Sensitivity to Little Age Ice timing in the weak mechanical regime

The diagram of simple LIA growth and collapse that is shown in Fig. 2b (Neoglacial IV) assumes that a 380-year growth phase is initiated in AD 1400 and that a maximum is achieved during the late 19th century. These assumptions are consistent with regional observations (Warren & Sugden 1993; Warren 1993; Villalba 1994; Aniya 1995). It is of interest to investigate the influence of a shorter growth phase. Such a case is computed with the same initiation date, but with equivalent epochs (300 yr) for accumulation and ablation. In this case the maximum is achieved in AD 1700 and the result is shown in Fig. 12(c). Indeed, the di erence in the resulting prediction for Type 2 is dramatic (compare predictions with either Fig. 12(a) or 12(b), which assume the same mantle viscosity and lithospheric thickness). Although the loading is of su cient duration (300 yr) to place the mechanical system far from equilibrium at the year AD 1700, the total 300-year ice mass wasting (unloading) is su cient to cause rebound (uplift) at all wavelengths at the present day. Our preferred model, however, has a longer growth phase, as portrayed in Figs 2(a) and (b). Finally, in Fig. 13 we show predictions for Types 1 and 2 Neoglaciations for the lowest mantle viscosity value considered here ($\eta = 5 \times 10^{18}$ Pa s). Here all memory of the LIA growth phase is dwarfed by the robust isostatic response to 20th century deglaciation.

What we have learned from these numerical experiments with realistic, yet simple, Patagonian LIA loading histories is that the lower end of the viscosity spectrum contains a rich assortment of response patterns and styles. These may involve either subsidence or uplift at the present day.

6.4 Summary of results

Viscoelastic memory dominates over the purely elastic deformation rate predictions for all realistic ranges of viscosity. This conclusion is in some conflict with the model results of Trupin *et al.* (1996), who computed uplift rates in the North American Cordillera caused by the combined influence of LGM, an AD 1650–1900 LIA and 20th century regional glacial recession. The main di erence, however, can be attributed to the di erent total volume rates of recession assumed by the models during the 20th century. Trupin *et al.* (1996) assumed glacial wasting in the northern Cordillera (including Alaska), which alone, accounts for the entire 0.4 mm yr^{-1} rate of sea level rise that Meier (1984) found plausible for the total worldwide system of small mountain glaciers and ice caps. In marked contrast, the estimate of Aniya *et al.* (1997) for South America's southernmost Cordillera, which is assumed here, accounts for approximately 1/20th of the total small mountain glacier contribution to sea level rise. The estimate of Aniya *et al.* (1997) is consistent with the values that Meier (1984) derived for southern Patagonia from scaling well-measured alpine glacial systems.

6.4.1 Weak mechanical regime

There is considerable sensitivity of the predicted uplift to the details of the LIA load history for cases where the viscosity is in the range 5.0×10^{18}–5.0×10^{19} Pa s and the lithosphere is relatively thin. This regime may be akin to that proposed for extensional continental tectonic environs such as the Basin

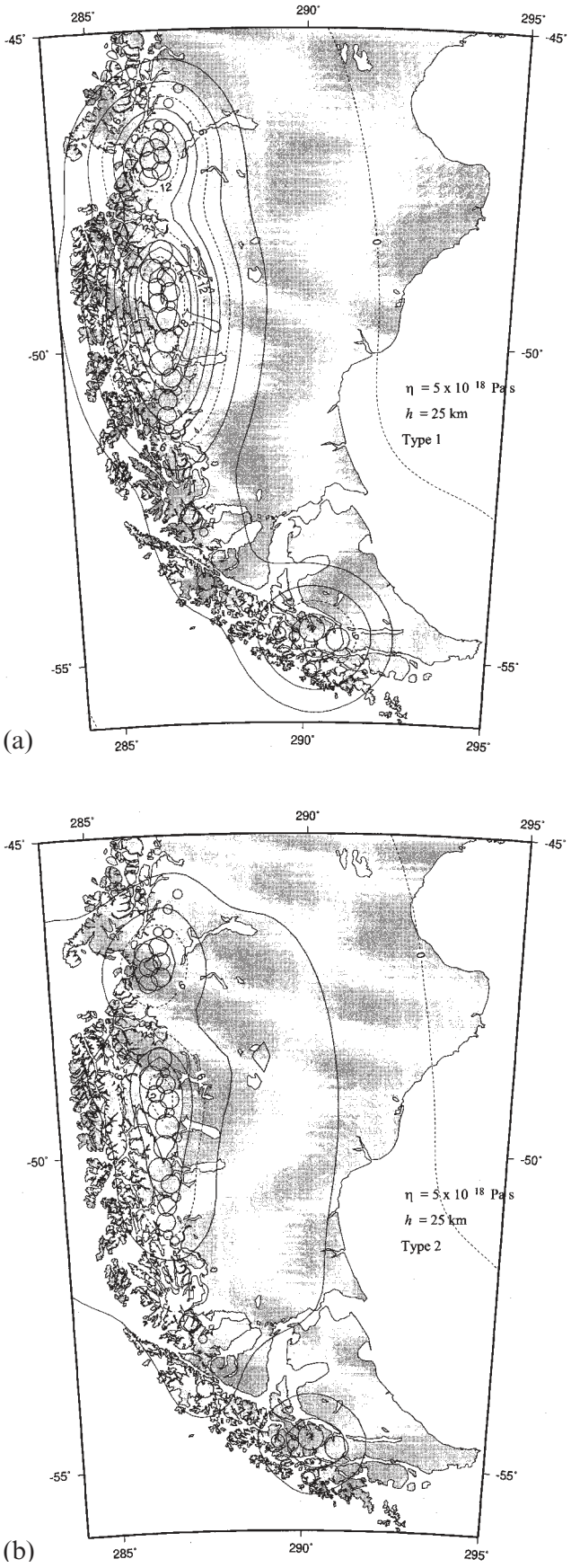

Figure 13. Predicted vertical velocity for cases identical to (a) and (b) of Fig. 12, but with viscosity reduced by a factor of 2.

and Range province of western North America (Bills *et al.* 1994). In this mechanical regime, present-day peripheral uplift (subsidence?) rates may be dramatic and peripheral bulge deformation could be unusually pronounced. Such an exotic deformation style is explained as a phase-lagged viscoelastic motion, in which the forcing frequency (period of Holocene glacial fluctuations) is comparable to the inherent relaxation decay times of the earth structure model. Geodetic observation of vertical displacement within the inner depression zone (near the load) will be highly sensitive to both the details of earth structure and timing of the LIA growth and collapse. The predicted results have shown that both uplift and subsidence may be predicted, or a near-cancellation of e ects might occur. There is some analogy to a stationary wave that is either phase-lagged (subsidence at the present day), in-phase (uplift at the present-day) or in a state of transition (giving a near-zero rate), in which out-of-phase behaviour (subsidence) is waning and will, in the future, be replaced by in-phase (uplift) as glacial collapse continues. This finding is consistent with the modelling results reported by Wolf *et al.* (1997), who also included the e ect of a finite-depth low-viscosity asthenospheric layer just below the lithosphere. Future studies of Patagonian isostasy should consider mantle viscous stratification and lateral heterogeneity as these may a ect the predicted regional patterns of crustal motion.

6.4.2 *Strong mechanical regime*

For a mantle viscosity that is comparable to that of Fennoscandia, any sensitivity to the details of late Holocene Neoglaciation is insignificant (see Figs 6a and b). In fact, in this viscosity range ($\eta \geq 6.5 \times 10^{20}$ Pa s) the present-day vertical motions are likely to be small unless the glacial mass involved in the Neoglaciation or that in the present-day deterioration of the SPI and NPI complexes has been grossly underestimated. For either Type 1 or Type 2 Neoglacial models, the maximum rates are of the order of 1 mm yr^{-1} of subsidence. The subsidence reflects the time-integrated load. Elastic rebound, which occurs as an instantaneous response to glacial mass changes, is predicted to be of much smaller magnitude and to have a contribution (uplift) that opposes that of viscoelasticity in both the stronger ('Fennoscandian') and intermediate ('Australian') mechanical regimes. Crustal motion induced by Neoglaciations in the stronger mechanical regime are probably undetectable using space geodesy. The story, however, is quite di erent if the mantle viscosity is reduced by a factor of 10, or more, below that of stable cratonic mantle.

Although environmental and solid Earth parameters are poorly known, our numerical study indicates that late Holocene Neoglaciation of southern Patagonia may drive present-day crustal motion at detectable levels (≥ 4 mm yr^{-1}), given current estimates of formal errors in the vertical associated with continuous GPS satellite tracking data (Zumberge *et al.* 1997). The relative absence of vertical neotectonic activity south of 46°30′S (Ramos & Kay 1992) suggests that a glacial isostatic signal may stand out above that associated with vertical tectonic motions by an order of magnitude or more.

7 CONCLUSIONS

Glacial moraines of the vast icefields of the southernmost Andean Cordillera record several periods of advance and retreat during mid- and late Holocene time. These regional glacial changes may be related to variations in precipitation and atmospheric temperature (Hulton *et al.* 1994; Naruse *et al.* 1995). Four ^{14}C dated Neoglacial advances and retreats of the Patagonian icefields during the last five millennia (Rabassa & Clapperton 1990; Aniya 1995) are modelled as ice loads that force viscoelastic gravitational deformation of the solid Earth. Our numerical models illustrate that significant vertical motion (2–20 mm yr^{-1}) might be occurring at the present day if the rates of glacial mass wasting determined by Aniya *et al.* (1997) represent a continuous recession of the Patagonian icefields from a Little Ice Age maximum *and* if the local mantle viscosity is similar to that estimated for regions sustaining Neogene tectonism.

We speculate that this lower viscosity regime is very likely to exist in southern Patagonia due to the subduction of oceanic ridge segments at 6–14 Ma and subsequent eruption of relatively large volumes of tholeiitic lavas and the creation of an upper-mantle slab window (Gorring *et al.* 1997). The three southwesternmost Argentine towns shown in Fig. 6(b) are located within the Magellan Basin, a region of recent tectonic extension (Diraison *et al.* 1997). The icefields are located within the Austral Volcanic Zone, a region with numerous Plio-Pleistocene-age eruptive magmas. Geochemical analyses of these magmas indicate melting of both sediment and basalt within the subducting Antarctic plate and melting of both mantle wedge and crustal rocks located above the slab (Stern & Kilian 1996). Peacock *et al.* (1994) argued that Pleistocene/Holocene magma genesis in this region involved the release of structurally bound H_2O at depth. Such active slab dehydration implies a relatively low mantle viscosity due to the sensitivity of α-phase olivine rheology to trace content of water (Hirth & Kohlstedt 1996; Chen *et al.* 1998).

Details of a Little Ice Age glacial advance and subsequent recession, such as the duration at maximum and timing of glacial recession, complicate the classic picture of glacial isostatic adjustment for low viscosities, ranging from 5×10^{18}–10^{20} Pa s. The vertical response of a phase-lagged viscoelastic Earth to Little Ice Age deglaciation can be either positive (emergent) or negative (submergent) at the present day. The latter predictions are in substantial agreement with recent Little Ice Age modelling of the Vatnajökull ice cap in Iceland by Wolf *et al.* (1997). In sum, the map view crustal motion predictions given in this paper illustrate that the trade-o of glacial load history during the last 500 years with Patagonian mantle viscosity is more complex than initially anticipated.

ACKNOWLEDGMENTS

This work was performed at the Jet Propulsion Laboratory, California Institute of Technology, under contract with NASA, and at the Pacific Geoscience Centre, an o ce of the Geological Survey of Canada. The JPL Supercomputing O ce has provided support of its facilities. A grant from the Solid Earth and Natural Hazards Program of NASA's Earth Science O ce has provided support for this research. Correspondence and conversations with Detlef Wolf are most gratefully acknowledged. Detlef Wolf, Carol A. Raymond, Gilles Peltzer, Paul Lundgren, Xiaoping Wu, Kenneth Hurst and Eric Rignot are thanked for comments and suggestions related to this research. Patrick Wu, Ralph Currie and Masamu Aniya have also provided useful comments on the manuscript. Geological Survey of Canada Contribution 1998120.

REFERENCES

Amelung, F. & Wolf, D., 1994. Viscoelastic perturbations of the Earth: significance of the incremental gravitational force in models of glacial isostasy, *Geophys. J. Int.,* **117,** 864–879.

Aniya, M., 1988. Glacier inventory for the Northern Patagonian Icefield, Chile, and variations 1944/45 to 1985/86, *Arctic Alp. Res.,* **20,** 179–187.

Aniya, M., 1995. Holocene glacial chronology in Patagonia: Tyndall and Upsala glaciers, *Arctic and Alpine Res.,* **27,** 311–322.

Aniya, M., Sato, H., Naruse, R., Skvarca, P. & Casassa, G., 1996. The use of satellite and airborne imagery to inventory outlet glaciers of the Southern Patagonian Icefield, South America, *Photogrammetric Eng. Remote Sensing,* **62,** 1361–1369.

Aniya, M., Sato, H., Naruse, R., Skvarca, P. & Casassa, G., 1997. Recent glacier variations in the Southern Patagonian Icefield, South America, *Arctic Alp. Res.,* **29,** 1–12.

Bills, B.G., Currey, D.R. & Marshall, G.A., 1994. Viscosity estimates for the crust and upper mantle from patterns of lacustrine shoreline deformation in the eastern Great Basin, *J. geophys. Res.,* **99,** 22 059–22 086.

Boninsegna, J.A., 1995. South American dendroclimatological records, in *Climate Since A.D. 1500,* pp. 446–462, eds Bradley, R.S. & Jones, P.D., Routledge, New York.

Broecker, W.S., 1966. Glacial rebound and the deformation of the shorelines of proglacial lakes, *J. geophys. Res.,* **71,** 4777–4783.

Candie, S.C. & Leslie, R.B., 1986. Late Cenozoic tectonics of the southern Chile Trench, *J. geophys. Res.,* **91,** 471–496.

Chen, J., Inoue, T., Weidner, D.J., Wu, Y. & Vaughan, M.T., 1998. Strength and water weakening of mantle minerals, olivine, wadsleyite and ringwoodite, *Geophys. Res. Lett.,* **25,** 575–578.

Clapperton, C.M. & Sugden, D.E., 1983. On Late-glacial and Holocene glacier fluctuations in maritime West Antarctica, in *Late- and Postglacial Oscillations of Glaciers: Glacial and Periglacial Forms,* pp. 283–290, ed. Schroeder-Lanz, H, A.A. Balkema, Rotterdam.

Clapperton, C.M. & Sugden, D.E., 1988. Holocene glacier fluctuations in South America and Antarctica, *Quat. Sci. Rev.,* **7,** 185–198.

Clapperton, C.M., Sugden, D.E., Kaufman, D.S. & McCulloch, R.D., 1995. The Last Glaciation in Central Magellan Strait, southernmost Chile, *Quat. Res.,* **44,** 133–148.

Clark, J.A., 1980. A numerical model of worldwide sea level changes on a viscoelastic Earth, in *Earth Rheology, Isostasy and Eustasy,* pp. 525–534, ed. Mörner, N.A., Wiley Interscience, New York.

Dirac, P.A.M., 1958. *The Principles of Quantum Mechanics,* Oxford University Press, London.

Diraison, M., Cobbold, P.R., Gapais, D. & Rossello, E.A., 1997. Magellan Strait: part of a Neogene rift system, *Geology,* **25,** 703–706.

Farrell, W.E., 1972. Deformation of the Earth by surface loads, *Rev. Geophys.,* **10,** 761–797.

Giunchi, C., Spada, G. & Sabadini, R., 1997. Lateral viscosity variations and postglacial rebound: e ects on present-day VLBI baselines, *Geophys. Res. Lett.,* **24,** 13–16.

Goes, S., Govers, R., Schwartz, S. & Furlong, K.P., 1997. 3-D modeling for the Mendocino Triple Junction area, *Earth planet. Sci. Lett.,* **148,** 45–57.

Gorring, M.L., Kay, S.M., Zeitler, P.K., Ramos, V.A., Rubiolo, D., Fernandez, M.I. & Panza, J.L., 1997. Neogene Patagonian plateau lavas: continental magmas associated with ridge collision at the Chile Triple Junction, *Tectonics,* **16,** 1–17.

Hamza, V.M. & Muñoz, M., 1996. Heat flow map of South America, *Geothermics,* **25,** 599–616.

Hansen, J. & Lebede , S., 1987. Global trends of measured surface air temperature, *J. geophys. Res.,* **92,** 13 345–13 372.

Heusser, C.J., 1989. Southern Westerlies during the last glacial maximum, *Quat. Res.,* **31,** 423–425.

Heusser, C.J. & Streeter, S., 1980. A temperature and precipitation record of the past 16 000 years in southern Chile, *Science,* **210,** 1345–1347.

Heusser, C.J., Denton, G.H., Hauser, A., Andersen, B.G. & Lowell, T.V., 1996. Water fern (Azolla *filiculoides* Lam.) in southern Chile as an index of paleoenvironment during early deglaciation, *Arctic Alp. Res.,* **28,** 148–155.

Hirth, G. & Kohlstedt, D.L., 1996. Water in the oceanic upper mantle: implications for rheology, melt extraction and the evolution of the lithosphere, *Earth planet. Sci. Lett.,* **144,** 93–108.

Hsui, A., 1981. Some remarks on the thermal consequences of ridge subduction, *Geophys. Res. Lett.,* **8,** 1031–1034.

Hulton, N., Sugden, D., Payne, A. & Clapperton, C., 1994. Glacier modeling and the climate of Patagonia during the last glacial maximum, *Quat. Res.,* **42,** 1–19.

Hutter, K., 1983. *Theoretical Glaciology,* D. Reidel, Dordrecht.

Huybrechts, P., 1992. The Antarctic ice sheet and environmental change: a three-dimensional modeling study, *Ber. Polarforsch.,* **99,** 1–241.

Ivins, E.R., 1996. Transient creep of a composite lower crust: 2. A polymineralic basis for rapidly evolving post-seismic deformation modes, *J. geophys. Res.,* **101,** 28 005–28 028.

Ivins, E.R. & Sammis, C.G., 1995. On lateral viscosity contrast in the mantle and the rheology of low-frequency geodynamics, *Geophys. J. Int.,* **123,** 305–322.

Jaeger, J.C., 1969. *Elasticity, Fracture and Flow with Engineering and Geological Applications,* Chapman & Hall, London.

James, T.S., 1991. Post-glacial deformation, *PhD thesis,* Princeton University, Princeton.

James, T.S. & Ivins, E.R., 1998. Predictions of Antarctic crustal motions driven by present-day ice sheet evolution and by isostatic memory of the Last Glacial Maximum, *J. geophys. Res.,* **103,** 4993–5017.

Johnston, P., Lambeck, K. & Wolf, D., 1997. Material versus isobaric internal boundaries in the Earth and their influence on postglacial rebound, *Geophys. J. Int.,* **129,** 252–268.

Jones, P.D., Raper, S.C.B. & Wigley, T.M.L., 1986. Southern Hemisphere surface air temperature variations: 1851–1984, *J. Climate appl. Meteorology,* **25,** 1213–1230.

Kaufmann, G. & Wolf, D., 1996. Deglacial land emergence and lateral upper-mantle heterogeneity in the Svalbard Archipelago: 2. Extended results for high-resolution load models, *Geophys. J. Int.,* **127,** 125–140.

Lambeck, K., 1993. Glacial rebound of the British Isles—II. A high-resolution, high-precision model, *Geophys. J. Int.,* **115,** 960–990.

McConnell, R.K., 1965. Isostatic adjustment in a layered Earth, *J. geophys. Res.,* **70,** 5171–5188.

Maeda, Y., Nakada, M., Matsumoto, E. & Matsuda, I., 1992. Crustal tilting from Holocene sea-level observations along the east coast of Hokkaido in Japan and upper mantle rheology, *Geophys. Res. Lett.,* **16,** 857–860.

Matsu'ura, M. & Iwasaki, T., 1983. Study on coseismic and postseismic movements associated with the 1923 Kanto earthquake, *Tectonophysics,* **97,** 201–215.

Meier, M.F., 1984. Contribution of small mountain glaciers to global sea-level, *Science,* **226,** 1419–1421.

Mercer, J.H., 1970. Variations of some Patagonian glaciers since the Late-Glacial: II, *Am. J. Sci.,* **269,** 1–25.

Mercer, J.H., 1976. Glacial history of southernmost South America, *Quat. Res.,* **6,** 125–166.

Mercer, J.H., 1982. Holocene glacier variations in southern South America, *Striae,* **18,** 35–40.

Mitrovica, J.X., 1996. Haskell (1935) revisited, *J. geophys. Res.,* **101,** 555–569.

Mitrovica, J.X. & Peltier, W.R., 1991. A complete formalism for the inversion of postglacial rebound data: resolving power analysis, *Geophys. J. Int.,* **104,** 267–288.

Montagner, J.-P. & Tanimoto, T., 1991. Global upper mantle tomography of seismic velocities and anisotropies, *J. geophys. Res.,* **96,** 20 337–20 351.

Nakada, M. & Lambeck, K., 1989. Late Pleistocene and Holocene sea-level change in the Australian region and mantle rheology, *Geophys. J.,* **96,** 497–517.

Nakada, M. & Lambeck, K., 1991. Late Pleistocene and Holocene sea-level change; evidence for lateral mantle viscosity structure?, in *Glacial Isostasy, Sea-level and Mantle Rheology,* pp. 79–94, eds Sabadini, R., Lambeck, K. & Boschi, E., Kluwer, Dordrecht.

Naruse, R. & Aniya, M., 1992. Outline of glaciological researches in Patagonia, 1990, *Bull. Glacier. Res.,* **10,** 31–38.
Naruse, R., Aniya, M., Skvarca, P. & Casassa, G., 1995. Recent variations of calving glaciers in Patagonia, South America, revealed by ground surveys, satellite-data analyses and numerical experiments, *Anal. Glaciology,* **21,** 297–303.
Oerlemans, J., 1997. Climate sensitivity of Franz Joseph Glacier, New Zealand, as revealed by numerical modeling, *Arctic Alp. Res.,* **29,** 233–239.
Peacock, S.M., Rushmer, T. & Thompson, A.B., 1994. Partial melting of subducting oceanic crust, *Earth planet. Sci. Lett.,* **121,** 227–244.
Peltier, W.R., 1974. The impulsive response of a Maxwell Earth, *Rev. Geophys. Space Phys.,* **12,** 649–668.
Peltier, W.R., 1976. Glacial-isostatic adjustment—II. The inverse problem, *Geophys. J. R. astr. Soc.,* **46,** 669–705.
Porter, S., 1981. Pleistocene glaciation in the southern Lake District of Chile, *Quat. Res.,* **16,** 263–292.
Rabassa, J. & Clapperton, C.M., 1990. Quaternary glaciations of the southern Andes, *Quat. Sci. Rev.,* **9,** 153–174.
Ramos, V.A. & Kay, S.M., 1992. Southern Patagonian plateau basalts and deformation: backarc testimony of ridge collisions, *Tectonophysics,* **205,** 261–282.
Sabadini, R.C.A., Yuen, D.A. & Boschi, E., 1984. A comparison of the complete and truncated versions of the polar wander equations, *J. geophys. Res.,* **89,** 7609–7620.
Sigmundsson, F., 1991. Postglacial rebound and asthenospheric viscosity in Iceland, *Geophys. Res. Lett.,* **18,** 1131–1134.
Sneddon, I.H., 1972. *The Use of Integral Transforms,* McGraw-Hill, New York.
Steinberger, B. & O'Connell, R.J., 1998. Advection of plumes in mantle flow: implications for hotspot motion, mantle viscosity and plume distribution, *Geophys. J. Int.,* **132,** 412–434.
Stern, C.R. & Kilian, R., 1996. Role of the subducted slab, mantle wedge and continental crust in the generation of adakites from the Andean Austral Volcanic Zone, *Contrib. Mineral Petrol.,* **134,** 263–281.
Thompson, L.J., Mosley-Thompson, E., Dansgaard, W. & Grootes, P.M., 1986. The Little Ice Age as recorded in tropical Quelcaya ice cap, *Science,* **234,** 361–364.
Thorkelson, D.J., 1996. Subduction of diverging plates and the principles of slab window formation, *Tectonophysics,* **225,** 47–63.
Trupin, A.S., Easson, D.A. & Han, D., 1996. Vertical motion and ice thickness variation in western North America, *Geophys. Res. Lett.,* **23,** 253–256.
Tushingham, A.M. & Peltier, W.R., 1991. ICE-3G: A new global model of late Pleistocene deglaciation based upon geophysical predictions of postglacial relative sea-level, *J. geophys. Res.,* **96,** 4497–4523.
Vermeersen, L.L.A. & Vlaar, N.J., 1991. The gravito-elastodynamics of a pre-stressed Earth, *Geophys. J. Int.,* **104,** 555–563.
Villalba, R., 1990. Climate fluctuations in Northern Patagonia during the last 1000 years as inferred from tree ring records, *Quat. Res.,* **34,** 346–360.
Villalba, R., 1994. Tree-ring and glacial evidence from the Medieval Warm Epoch and the Little Ice Age in southern South America, *Climate Change,* **26,** 183–197.
Walcott, R.I., 1970. Isostatic response to loading of the crust in Canada, *Can. J. Earth Sci.,* **7,** 716–729.
Ward, S.N., 1984. A note on lithospheric bending calculations, *Geophys. J. R. Astr. Soc.,* **78,** 241–253.
Warren, C.R., 1993. Rapid recent fluctuations of the calving San-Rafael glacier, Chilean Patagonia: climatic or non-climatic?, *Geografiska Annal.,* **75A,** 111–125.
Warren, C.R. & Sugden, D.E., 1993. The Patagonian icefields: a glaciological review, *Arctic Alp. Res.,* **25,** 316–331.
Wolf, D., 1984. The relaxation of spherical and flat Maxwell Earth models and e ects due to the presence of the lithosphere, *J. Geophys.,* **56,** 24–33.
Wolf, D., 1985a. The normal modes of a layered, incompressible Maxwell half-space, *J. Geophys.,* **57,** 106–117.
Wolf, D., 1985b. The normal modes of a uniform, compressible Maxwell half-space, *J. Geophys.,* **56,** 100–105.
Wolf, D., 1993. The changing role of the lithosphere in models of glacial isostasy: a historical review, *Global planet. Change,* **8,** 95–106.
Wolf, D., Barthelmes, F. & Sigmundsson, F., 1997. Predictions of deformation and gravity caused by recent change of Vatnajökull ice cap, Iceland, *Comp. Rend. J. Luxemb. Geodyn.,* **82,** 36–42.
Zumberge, J.F., Heflin, M.B., Je erson, D.C., Watkins, M.M. & Webb, F.H., 1997. Precise point positioning for e cient and robust analysis of GPS data from large networks, *J. geophys. Res.,* **102,** 5005–5017.

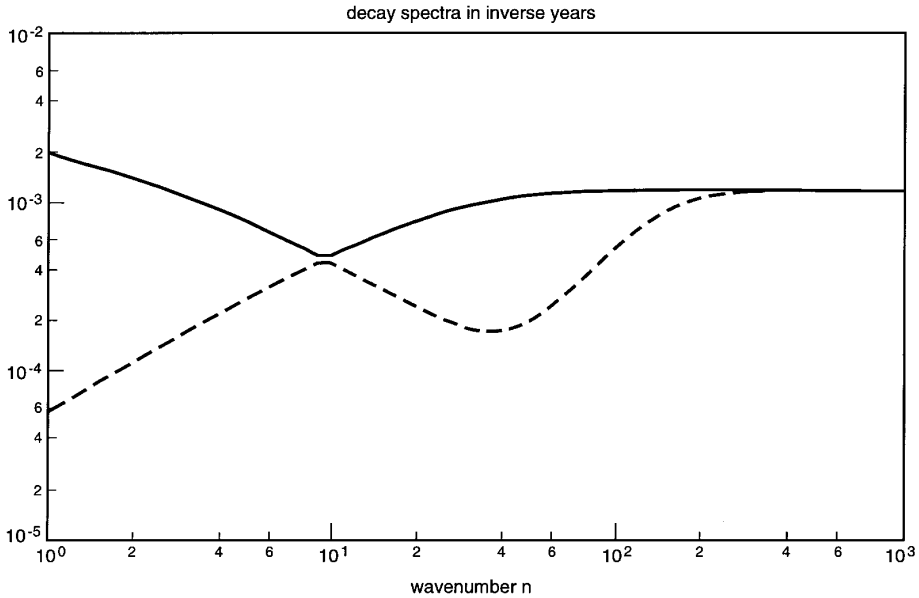

Figure A1. Relaxation spectra for half-space viscosity $\eta = 0.75 \times 10^{21}$ Pa s and $h = 100$ km (elastic layer thickness). The wavenumber n is identical to that employed by Wolf (1985a), in which $n(k') \equiv k'(R/h)$, where R is the Earth's radius. Solid line is γ_1 and dashed line γ_2. Note the near-degeneracy for $n > 3 \times 10^2$. Model density structure is $\rho_1 = 2.9$ gm cm^{-3} and $\rho_2 = 3.9$ gm cm^{-3}. Elastic shear moduli are $\mu_1^e = 44.1$ GPa and $\mu_2^e = 75.0$ GPa.

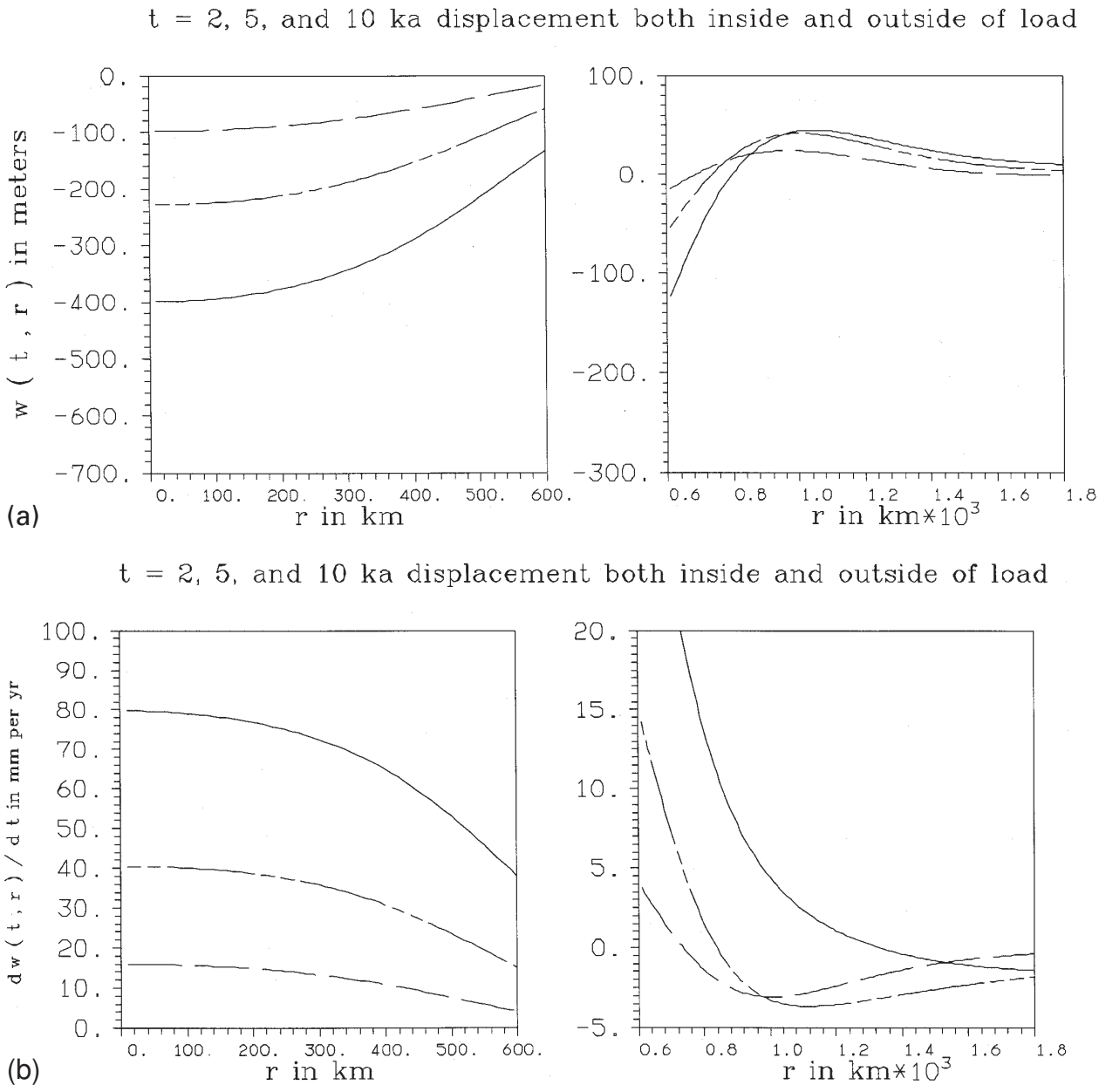

Figure A2. Surface vertical displacement field, $w_0(r, t)$, for benchmark comparison case (a). Load history is simulated as in Fig. 4(b) with $\alpha = 600$ km, $t_1 = 1.0$, $t_2 = 2000.0$, $t_3 = 2000.1$ (units kyr) and $h_{0,1} = h_{0,2} = 2.0$ km, $h_{0,3} = 0.0$ km with $\rho_0 = 1.0$ gm cm^{-3}. Assumed earth model parameters are $h = 100$ km, $\rho_1 = 3.36$ gm cm^{-3}, $\rho_2 = 3.38$ gm cm^{-3}, $\mu_1^e = 67$ GPa, $\mu_2^e = 145$ GPa and $\eta = 1.0 \times 10^{21}$ Pa s. Frame (b) shows rates at the same set of times as (a) after complete load removal: 2 ka (solid curve), 5 ka (double-short, single long-dashed curve) and 10 ka (even-dashed curve). Frame (c) shows vertical displacement for a load history as in Fig. 4(b) with $t_1 = 10^{-4}$, $t_2 = 2 \times 10^{-4}$, $t_3 = 2500$ ka and $h_{0,2} = h_{0,3} = 3.0$ km, $h_{0,1} = 1.5$ km. Frame (c) has all parameters identical to (a) and (b) except $\alpha = 800$ km, $\rho_1 = 3.32$ gm cm^{-3} and $\rho_2 = 3.34$ gm cm^{-3}. Evaluation times in frame (c) are $t = 3 \times 10^{-4}$ (≈ 0), $t = 1.0003$ and $t = 2400$ kyr ($\approx \infty$), with solid, double-short and single-dashed curves for progressively longer evaluation times. [See also Fig. 10 of Wolf (1985a) and Fig. 6 of Wolf (1984) for comparison.] Frames (a)–(c) assume square-edged disc load in contrast to (d), which is for a load of elliptical cross-section. Frame (d) has all other parameters identical to (c).

APPENDIX A: COMPARISON OF SPHERICAL AND PLANAR VERTICAL DEFORMATION SOLUTIONS

In this Appendix we briefly describe two important features of the theoretical model discussed and developed in Section 5. First, the model can be directly compared to the results of Wolf (1984, 1985a,b). Fig. A1 shows the decay spectra, γ_p, in inverse years. A characteristic 'hummingbird' shape in wavenumber–eigenvalue space is revealed. This character underlies the response of a simple elastic lithosphere welded to a viscoelastic half-space. Fig. A2 shows the surface vertical response for a single disc load having a Heaviside unit step function character in time. The cases shown in Fig. A2

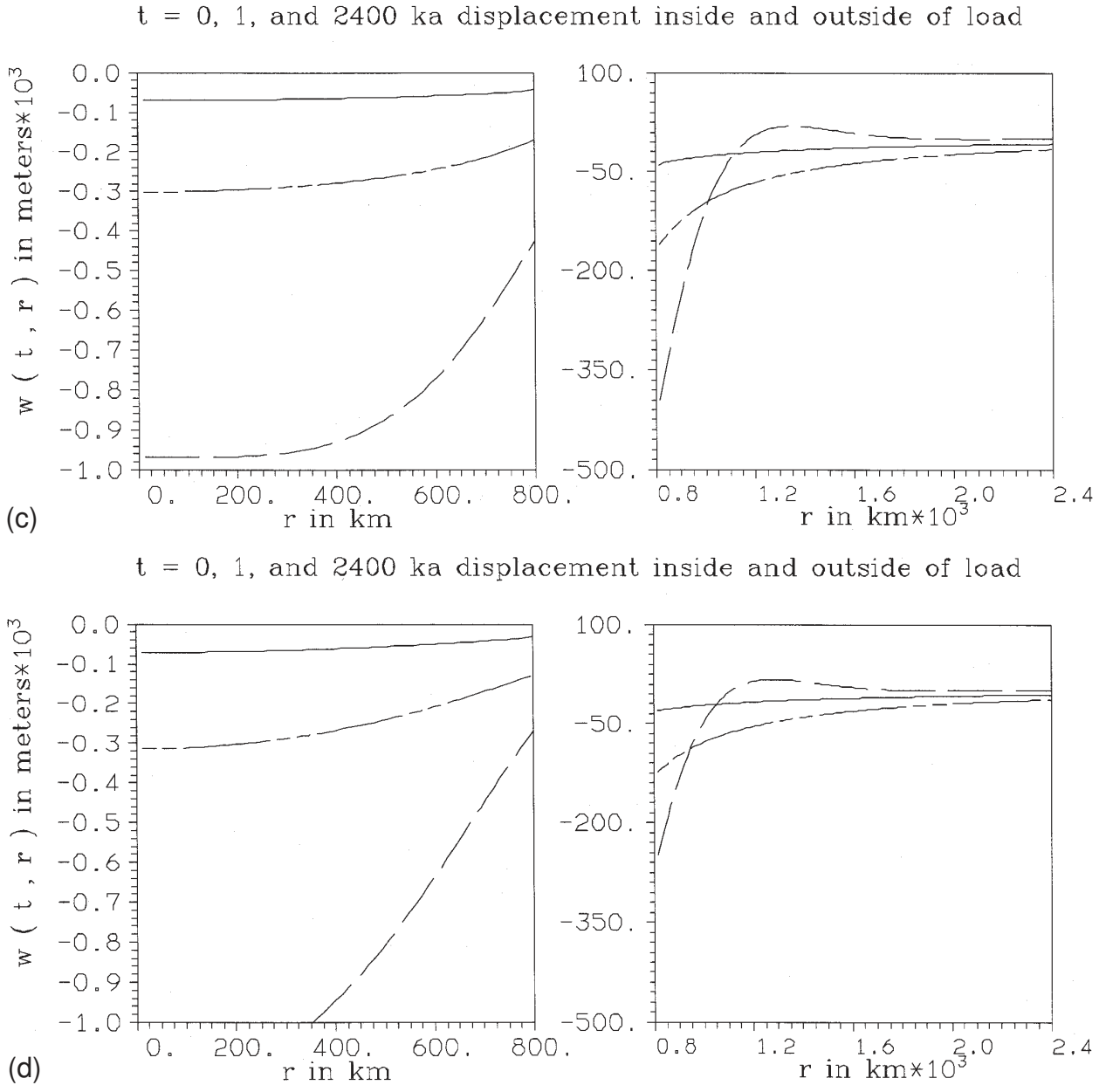

Figure A2. (*Continued.*)

are directly comparable to the computational examples discussed by Wolf (1984, 1985a). Comparison to the latter examples reveals that they are essentially identical and that each may, therefore, be regarded as providing numerical benchmarks.

Second, we provide a comparison of predictions using both polar coordinate, planar geometry (this paper) and spherical geometry. The latter predictions are constructed using a radially layered incompressible Maxwell model developed by James (1991) after the method of Sabadini *et al.* (1984). This provides an assessment of the level of error that is engendered by adoption of a flat-earth approximation for the calculation of postglacial isostatic adjustment. Thus, we provide an extension of the work of Wolf (1984) and Amelung & Wolf (1994), who studied the di erences in response of spherical and flat-earth models. The comparison here is performed for the case of ICE-3G deglaciation of the Patagonian region. The spherical theory employed assumes finite self-gravitational terms. The latter terms are relevant to such comparisons, as noted by Amelung & Wolf (1994). Fig. A3(a) shows the di erence between spherical and flat-earth calculations. The total surface displacement (in meters) is shown in Fig. A3(b) at 13 kyr BP, 2 kyr after the assumed termination of deglaciation in the ICE-3G model of Tushingham & Peltier (1991). The di erences are generally of the order of 1 per cent, with peak di erences at a 10 per cent level in the peripheral bulge zones

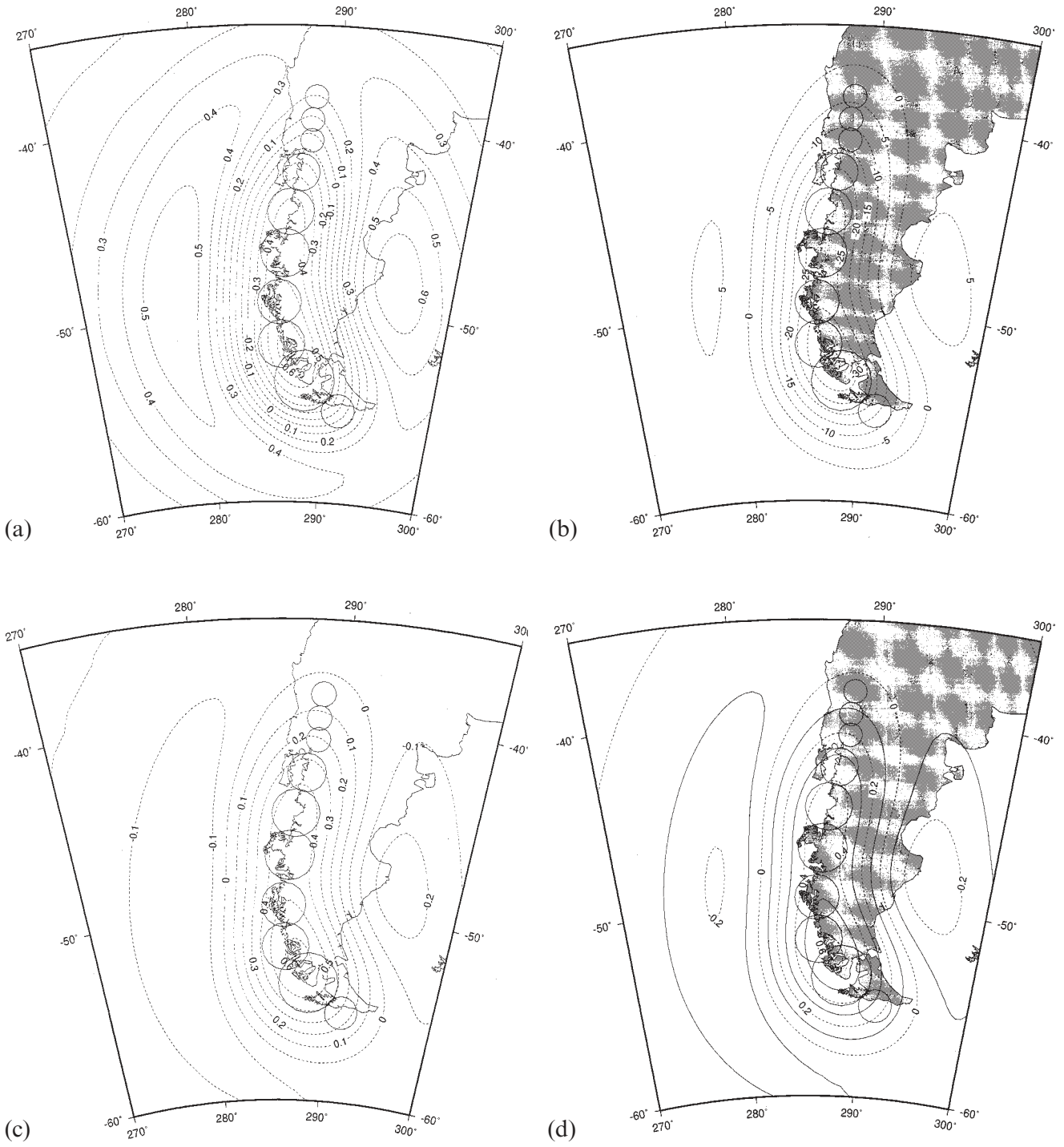

Figure A3. Comparison of spherical and flat-earth model computation. Load build-up phase assumes zero height at 108 kyr BP with subsequent linear ramp to ICE-3G heights at 18 kyr. All subsequent load history is identical to ICE-3G as in Tushingham & Peltier (1991). $\rho_0 = 1.0$ g cm^{-3}. Load heights are zero after 15 kyr. The earth parameters assumed are $h_1 = 100$ km, $\eta = 1.0 \times 10^{21}$ Pa s, $\mu_1^c = 67.0$ GPa, $\mu_2^c = 145.0$ GPa, $\rho_1 = 3.38$ g cm^{-3}, $\rho_2 = 3.39$ g cm^{-3} and $g = 9.832186$ m s^{-2}. Frame (a) shows the di erence in vertical displacement at 13 ka. Frame (b) shows the amplitude and sign of the solution for the flat-earth assumption. Frames (c) and (d) show the present-day uplift rate for spherical and flat-earth models, respectively. Spherical harmonic truncation level is $n = 240$. Note the remarkable similarity of the rate of uplift magnitude and pattern in frames (c) and (d).

(5 m lobate-shaped uplift in the Pacific and Atlantic oceans). Figs A3(c) and (d) show the ICE-3G isostatic uplift rates at the present day for spherical and flat-earth models, respectively. The spherical earth model was computed at degree 480 truncation for resolution testing. The spherical model is well resolved at degree truncation 240. The comparison demonstrates that the flat-earth approximation is su ciently accurate over 20° of Earth surface.